MAGNETIC CHARACTERIZATION OF EXPANDED AUSTENITE PHASE FORMED ON NITROGEN ION IMPLANTED 316 STAINLESS STEEL ALLOY

A Thesis Submitted to
the Graduate School of Engineering and Sciences of
İzmir Institute of Technology
in Partial Fulfillment of the Requirements for the Degree of

MASTER OF SCIENCE

in Materials Science and Engineering

by
Özgün KARATAŞ

January 2015
İZMİR

We approve the thesis of **Özgün KARATAŞ**

Examining Committee Members:

_____

Prof. Dr. Orhan ÖZTÜRK
Department of Physics, İzmir Institute of Technology

_____

Prof. Dr. Ahmet ÖZTARHAN
Department of Electronics and Communication Engineering, İzmir University

_____

Prof. Dr. İbrahim AVGIN
Department of Electrical and Electronics Engineering, Ege University

9 January 2015

_____

Prof. Dr. Orhan ÖZTÜRK
Supervisor, Department of Physics,
İzmir Institute of Technology

_____

Prof. Dr. Mustafa M. DEMİR
Head of the Department of
Materials Science and Engineering

_____

Prof. Dr. Bilge KARAÇALI
Dean of the Graduate School of
Engineering and Sciences

ACKNOWLEDGEMENTS

First of all, I would like to express my gratitude to my advisor Prof. Dr. Orhan Öztürk. His guidance, encouragement, advices, patience and teaching made me always feel confident throughout my study.

I would like to thank Prof. Dr. Don L. Williamson and his research group from Department of Physics, Colorado School of Mines for providing Ni implanted 316 stainless steel specimens and carrying out the implantation processes.

Another thanks goes to staff of Material Research Center of Izmir Institute of Technology for their contribution and help during characterization part of my study.

I would like to thank Department of Physics of Gebze Institute of Technology for facilitating MOKE analysis in their laboratories and Erdem Demirci for his help during the analysis.

I also would like to thank my colleague and friend Refika Dal. Her invaluable help and support mean a lot to me during my study.

Finally, the biggest thanks goes to my family. No word can explain their contributions to my life. I am very grateful to them for their endless support, devotions, understanding and more countless helps. I consider myself lucky to have them.

ABSTRACT

MAGNETIC CHARACTERIZATION OF EXPANDED AUSTENITE PHASE FORMED ON NITROGEN ION IMPLANTED 316 STAINLESS STEEL ALLOY

Austenitic stainless steels (SSs) are technologically important alloys and highly resistant to corrosion in a variety of environments. Nevertheless, these materials have a few drawbacks; they are rather soft materials and susceptible to wear. Correspondingly, an improvement of the surface properties is often desirable. Ion beam techniques are widely used to enhance surface properties of these alloys. Surface modification of austenitic SSs by nitrogen ion beams at moderate substrate temperatures near 400 ºC, leads to the formation of a high N content phase. This phase, known as an expanded austenite phase, γ_N, creates a hard and wear resistant layer on the stainless steel. Additional property of this phase is related to its magnetic structure due to the large amount of nitrogen insertion and corresponding lattice expansion.

In the current study, new data corresponding to structural and magnetic nature of the expanded austenite layers on austenitic 316 SS by low-energy, high-flux nitrogen ion implantation are presented. Phase and compositional analyses, surface topography and magnetic features of the nitrogen ion implanted layers were studied by a combination of experimental techniques involving XRD, SEM, AFM, MFM, VSM and MOKE. Nitrogen implantations were performed for 30, 90 and 240 minutes of processing time, at a fixed temperature near 400 °C. Relatively low-energy (0.7 keV) and high-flux (2 mA/cm^2) ion beam conditions were carried out during the implantation.

Combination of the aforementioned techniques provides strong evidence for the formation of the γ_N phase with mainly ferromagnetic characteristics. MFM imaging reveals stripe-like domain structures of the nitrogen ion implanted layers. Both VSM and MOKE analyses display hysteresis loops of the layers. Ferromagnetism in the γ_N layers are manifested by MFM, VSM and MOKE analyses. Ferromagnetic structure is linked to large lattice expansions (~10 %) due to high nitrogen contents (~28 at. %). As an interstitial impurity, nitrogen dilates fcc lattice of 316 SS i.e. Fe-Fe distance is increased, which strongly influences the magnetic interactions.

ÖZET

AZOT İYONU İMPLANTE EDİLMİŞ 316 PASLANMAZ ÇELİK ALAŞIMINDA OLUŞAN GENİŞLETİLMİŞ ÖSTENİT FAZININ MANYETİK KARAKTERİZASYONU

Östenitik paslanmaz çelikler teknolojik olarak önemli alaşımlardır ve çeşitli ortamlarda korozyona karşı yüksek direnç gösterirler. Fakat yine de bu malzemelerin bazı eksiklikleri bulunmaktadır; oldukça yumuşak malzemelerdir ve aşınmaya karşı duyarlıdırlar. Buna bağlı olarak yüzey özelliklerinin iyileştirilmesi sıklıkla istenen bir durumdur. İyon demeti teknikleri bu malzemelerin yüzey özelliklerini geliştirmede geniş ölçüde kullanılmaktadır. Bu malzemelere iyon demeti teknikleri ile 400 ºC civarı altlık sıcaklığında azot yüzey modifikasyonu yapılması, yüksek N içerikli bir fazın oluşumuna yol açmaktadır. Genişlemiş östenit fazı (γ_N) olarak bilinen bu faz, paslanmaz çeliğin üzerinde sert ve aşınma direnci yüksek tabakalar oluşturur. Buna ilaveten bu fazın bir başka özelliği de yüksek miktarda azotun kafes yapısına girerek genişletmesinden dolayı oluşan manyetik yapısı ile bağıntılıdır.

Mevcut çalışmada, düşük-enerji yüksek-akım iyon implantasyonu yoluyla östenitik 316 paslanmaz çelik (316 SS) üzerinde oluşan genişlemiş östenit tabakalarının yapısal ve manyetik özelliklerine dair yeni veriler sunulmuştur. Azot iyon implante edilmiş tabakaların faz ve kompozisyon analizi, yüzey topografisi ve manyetik özellikleri, XRD, SEM, AFM, MFM, VSM ve MOKE'u içeren deneysel tekniklerin birleşimiyle incelenmiştir. Azot implantasyonları, yaklaşık 400 °C civarlarında sabit sıcaklıkta, 30, 90 ve 240 dakika işlem sürelerinde gerçekleştirilmiştir. Nispeten düşük enerji (0.7 keV) ve yüksek akım (2 mA/cm^2) iyon demeti koşulları uygulanmıştır.

Yukarıda bahsedilen teknikler yardımıyla, γ_N oluşumu ve başlıca ferromanyetik karakteristiğiyle ilgili güçlü bulgular sunulmuştur. MFM görüntüleme, azot implante edilmiş tabakaların şerit biçimli domen yapılarını ortaya koymuştur. VSM ve MOKE, bu tabakaların histeresis eğrilerini göstermiştir. MFM, VSM ve MOKE analizleri, γ_N tabakalarındaki ferromanyetizmanın varlığını açıkça sunmuştur. Ferromanyetik yapı, azot miktarına bağlı (atomca yaklaşık % 28) yüksek kafes genişlemeleriyle ilişkilendirilmiştir (yaklaşık % 10). Bir arayer safsızlığı olan azot, 316 SS alaşımının yüzey merkezli kübik kafes yapısını genişletmekte, diğer bir deyişle demir-demir atomları arası mesafe artmakta, bu da güçlü ölçüde manyetik etkileşime etki etmektedir.

To my Family

TABLE OF CONTENTS

LIST OF FIGURES

Figure **Page**

LIST OF TABLES

Table **Page**

CHAPTER 1

INTRODUCTION

Stainless steels are known for their high corrosion resistance in various environments especially in ambient atmosphere with their nickel and molybdenum content. Their predominant alloying element is chromium; a concentration of at least 11 wt. % Cr is required and they contain less than 1 wt. % carbon.

Stainless steels can be classified in three groups due to their basis of the predominant phase constituent of the microstructure—martensitic, ferritic or austenitic. Their microstructure is body centered tetragonal (bct), body centered cubic (bcc) and face centered cubic (fcc) crystal lattice, respectively. The application fields of stainless steels are broadened by changing the composition or adding several alloying elements such as cobalt, manganese, silicon, tungsten, chromium, titanium, vanadium, etc.

The focus of this study is 316 austenitic stainless steel. 316 stainless steel (SS) is basically an alloy of Fe, Cr, Ni with other impurities having fcc crystal structure. The elemental composition of this specific alloy is given in Table 1.1 both in weight and atomic percent.

Table 1.1. Elemental composition of 316 stainless steel

Elemental composition of 316 stainless steel												
	Fe	**Cr**	**Ni**	**Mo**	**Mn**	**Si**	**Cu**	**Co**	**N**	**P**	**S**	**C**
weight %	66,39	17,07	11,64	2,16	1,66	0,35	0,34	0,26	0,07	0,03	0,02	0,01
atomic %	66,11	18,26	11,03	1,25	1,68	0,69	0,30	0,25	0,28	0,05	0,04	0,06

Austenitic steels are widely used in numerous industrial applications such as biomedical, automotive, chemical, food, aeronautic and nuclear power stations. What makes them this favorable can be explained by their excellent corrosion and oxidation resistance, good ductility and weldability characteristics. In addition, they are capable to enhance hardness and strength by heat treatment processes. However, these materials are rather soft and exhibit moderate wear resistance.

316 SS might be used as stents, knee or hip implants in biomedical industry. Nevertheless, implant materials need to satisfy some certain requirements. High load-bearing capacity and good tribological properties are extremely important since implant is exposed to high body force and friction when placed in body. Secondly, metallic implant materials can release some toxic elements such as Co, Cr and Ni from the surface into the body, which may give rise to health concerns as intoxication effect over time. Last, as the implant interacts with body constituents, unavoidable corrosion and wear are observed on them resulting with crevice and fretting corrosion. Unless these issues are resolved, early fracture and failure may occur as a result.

Earlier studies show that there are several surface modification techniques offering to improve surface properties of austenitic stainless steel alloys. (Blawert, Kalvelage, Mordike, Collins, Short, Jirásková and Schneeweiss 2001, Riviere, Méheust, Villain, Templier, Cahoreau, Abrasonis and Pranevicius 2002, Chen, Li, Bell and Dong 2008, Wu, Kahn, Michal, Ernst and Heuer 2011, Martinavičius, Abrasonis, Scheinost, Danoix, Danoix, Stinville, Talut, Templier, Liedke and Gemming 2012). Surface modification by inserting nitrogen ions with plasma and ion implantation techniques is well established to enhance surface properties. Protective layers are formed on the surface of these alloys by modifying the near surface layers of these materials via these nitrogen ion beam surface modification methods. On top of nitrogen, carbon, oxygen, boron, silicon and inert ions (Ar, He) can be also used as surface modification element. However, nitrogen is more frequently used among them due to more favorable surface properties such as wear, corrosion resistances and fatigue resistance.

Surface modification by inserting nitrogen ions with plasma and ion implantation techniques comprises plasma nitriding, plasma immersion ion implantation (PIII) and conventional beam line ion implantation. The basic differences between them are the altering ion energy and relative fraction of energetic ions, electrons, thermal atoms and ions impinging on the surface (Roth 2001). Conventional ion implantation but with low energy, high-flux, was used in this study.

It is well-established that nitrogen incorporation into the surface of austenitic stainless steel alloys (304, 310, 316 SS) by a wide variety of surface modification techniques at a relatively low surface treatment temperature ranging between 350 - 400 °C leads to a metastable, **high-N phase**, γ_N, in the treated layers (Zhang and Bell 1985, Ichii, Fujimura and Takase 1986, Dearnley, Namvar, Hibberd and Bell 1989,

Williamson, Ozturk, Wei and Wilbur 1994). Nitrogen atoms occupy interstitial sites in fcc lattice in γ_N and expands the phase. So that, the phase is known as expanded austenitic phase. It seems that the term 'expanded austenite' was introduced by Singer and coworkers; the phase has also been called '**S phase**', **ε´** and '**m phase**'. High strength (hardness values as high as 20 GPa), good corrosion resistance and dramatically improved wear resistance under high loads are a few of the technologically important properties reported in the literature for the γ_N phase. This phase forms a protective, hard and wear resistant surface layer with enhanced corrosion resistance on austenitic stainless steels. In addition to this, there are some peculiar properties associated with this phase such as grain dependent N content and diffusion rate depending behavior resulting anisotropic lattice expansion and high residual stresses.

Another peculiar property of this expanded austenite phase is noteworthy: magnetic characteristics. Although austenitic steels generally behave as nonmagnetic at room temperature, the expanded phase is found to have ferromagnetic as well as paramagnetic characteristics depending on nitrogen content (20–30 at.%) and lattice expansions (as high as 10%).

Earlier studies of this phase were first started in 1986. K. Ichii et al. were first to report the magnetic feature of this phase. In their study, they nitrided 304 stainless steel at law temperatures (400 °C), and found that the nitrided layer was composed of the γ_N phase with ferromagnetic nature. A much later study under low-energy, high-flux N implantation conditions of 304 SS at 400 °C revealed many more details about the magnetic nature of the γ_N phase (Öztürk and Williamson 1995). Via conversion electron Mössbauer spectroscopy (CEMS) and magneto-optic Kerr effect (MOKE), their study demonstrated that the γ_N phase had the magnetic properties of a soft magnetic material and was distributed in the highest N concentration and associated lattice expansion region of the implanted layer. Furthermore, this study revealed that the γ_N phase transformed to the paramagnetic state deeper into the layer as the N content and lattice expansion decreased (Figure 1.1). The magnetic γ_N phase, was stabilized at room temperature by huge lattice expansions (caused by high N contents, approaching an apparent saturation limit of ~30 at.%, and residual stresses as high as 2 GPa) induced by the high beam fluxes at 400 °C.

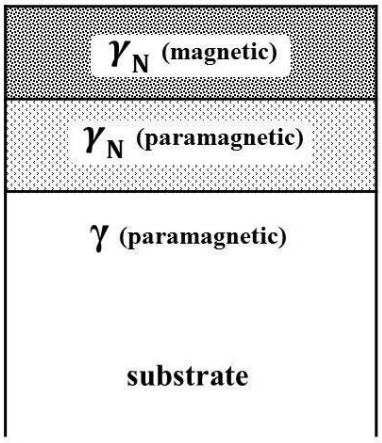

Figure 1.1. Decomposition of the γ_N layer into a few sublayers (2 layers in the figure).The top sublayer refers to the topmost γ_N layer having magnetic characteristics, whereas the second sublayer is paramagnetic corresponding to change of N amount with depth.

Two recent studies, involving ion and gas-phase nitrided 316 stainless steels (Basso, Pimentel, Weber, Marcos, Czerwiec, Baumvol and Figueroa 2009, Wu, Kahn, Michal, Ernst and Heuer 2011), however, find a lower threshold N content value, about 14 at.%, for the ferromagnetic expanded phase. A few earlier studies have reported the nitrogen profile reaches a concentration of about 20 at.% (Tian, Zeng, Zhang, Tang and Chu 2000) and above 17.5 at.% (Blawert, Kalvelage, Mordike, Collins, Short, Jirásková and Schneeweiss 2001) for this phase.

After the detailed study (Öztürk and Williamson 1995), a number of publications reported observations related to the magnetic character of the γ_N phase formed on austenitic SSs. More recently, the ferromagnetic nature of the γ_N phase in austenitic SS alloys was revealed through the observation of stripe-like domains via magnetic force microscopy (MFM) imaging and through the observation of hysteresis loops via magneto-optic Kerr effect (MOKE) (Fewell, Mitchell, Priest, Short and Collins 2000, Menéndez, Martinavicius, Liedke, Abrasonis, Fassbender, Sommerlatte, Nielsch, Suriñach, Baró and Nogués 2008, Öztürk, Okur and Riviere 2009, Menéndez, Stinville, Tromas, Templier, Villechaise, Rivière, Drouet, Martinavičius, Abrasonis and Fassbender 2010). In these studies, the origin of the ferromagnetism in the γ_N phase is mainly explained by large lattice expansions (due to high N content), and should eventually be related to the underlying origins of magnetic effect in fcc-Fe and related alloys. Some other researches correlate the ferromagnetism of the γ_N phase with various

defects (stacking faults, twins, etc.) observed in the expanded phase layers (Blawert, Kalvelage, Mordike, Collins, Short, Jirásková and Schneeweiss 2001).

Although the γ_N phase has been extensively investigated by various research groups, magnetic character of this phase has been lacking in earlier studies. It is noteworthy that this grain dependent magnetic feature on a non-magnetic substrate of these thin layers may be utilized in some industrial applications such as high density magnetic recording applications.

The focus of this study is to improve our understanding of magnetic characteristics of the expanded austenite phase on 316 SS by low energy, high-flux nitrogen ion implantation. Investigating topographical change, magnetic features, and surface compositional change and crystal structure of our N implanted phase via characterization methods will enable us to understand process time-dependent behavior of this phase. Surface crystal structures, surface topography and compositional change in depth will be investigated through using a combination of x-ray diffraction (XRD) and grazing incidence x-ray diffraction (GIXRD), scanning electron microscopy (SEM) and atomic force microscopy (AFM) and energy dispersive x-ray spectroscopy (EDS). Magnetic characterization plays a big role for the aim of this study. Three main methods will be used to characterize magnetic features of the expanded austenite phase: magnetic force microscopy (MFM), magneto-optic Kerr effect (MOKE) and vibrating sample magnetometer (VSM).

CHAPTER 2

MATERIALS AND EXPERIMENTAL METHODS

2.1. 316 Austenitic Stainless Steel Alloy

Austenitic stainless steels are alloys that are mainly composed of Fe, Cr and Ni. Stainless steels are normally classified into 3 groups on the basis of the predominant phase constituent of the microstructure; martensitic, ferritic, or austenitic depending at room temperature corresponding to a body centered tetragonal (bct), body centered cubic (bcc) and face centered cubic crystal (fcc) lattice, respectively. Both martensitic and ferritic stainless steels are magnetic; the austenitic stainless steels are not (Callister and Rethwisch 2012).

316 stainless steel (SS) is material to be nitrogen implanted in this study. It is an austenitic type steel composed mainly of Fe, Cr and Ni, and has face centered cubic (fcc) crystallographic structure. The crystal structure of 316 SS is represented in Figure 2.1. This illustration has been simulated via VESTA, a 3D visualization program. Polished disc specimens of 316 SS were implanted by a research group in Colorado School of Mines.

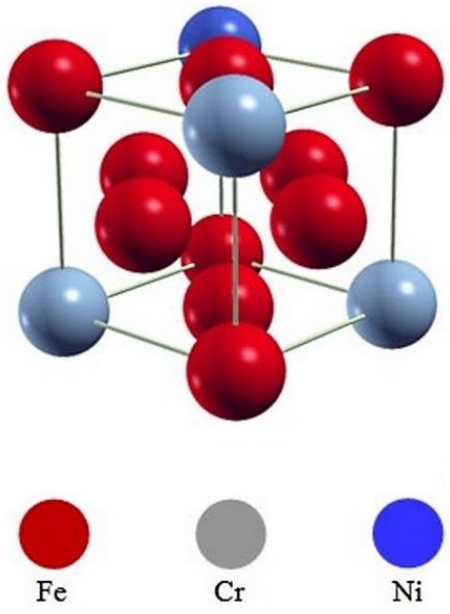

Figure 2.1. Schematic diagram of fcc-γ (Fe, Cr, Ni)

In this study, our austenitic steel is grade 316 stainless steel (AISI 316). Grade 316 is the standard molybdenum-bearing grade, second in importance to 304 amongst the austenitic stainless steels. The molybdenum addition provides grade 316 better overall corrosion resistant properties than grade 304, particularly higher resistance to pitting and crevice corrosion in chloride ion solutions (Table 2.1).

Table 2.1. Environmental properties of Grade 316 SS in various environments (1= Poor, 5= Excellent) (Source: CES EduPack Materials Selection Software 2009)

Environmental Properties					
Resistance Factors	**1**	**2**	**3**	**4**	**5**
Flammability					*
Fresh Water					*
Organic Solvents					*
Oxidation at 500 ^{0}C					*
Sea Water					*
Strong Acid					*
Strong Alkalis					*
UV					*
Wear				*	
Weak Acid					*
Weak Alkalis					*

It has excellent forming and welding characteristics. It is readily bent or roll formed into a variety of parts for applications in the industrial, transportation and medical fields. 316 SS also has outstanding welding characteristics. Post-weld annealing is not required when welding thin sections. Some mechanical and physical properties of 316 SS are listed in Table 2.2. The austenitic structure also gives this alloy excellent toughness, even down to cryogenic temperatures.

Table 2.2. Featured physical and mechanical properties of stainless steel AISI 316 in The International System (SI) of Units Ref. (Source: CES EduPack Materials Selection Software 2009)

	Minimum Value	Maximum Value	Units
Average Atomic Volume	0.0069	0.0072	m^3/kmol
Density	7.87	8.07	Mg/m^3
Fracture Toughness	112	278	$MPa.m^{1/2}$
Hardness	1700	2200	MPa
Poisson's Ratio	0.265		0.275
Tensile Strength	480	620	MPa
Young's Modulus	190	205	GPa
Max Service Temperature	1023	1198	K
Melting Point	1648	1673	K
Thermal Conductivity	13	17	W/m.K
Thermal Expansion	15	18	10^{-6}/K
Resistivity	69	81	10^{-8}ohm.m

2.2. Sample Preparation

In this study conventional beam line ion implantation technique was carried out in order to implant nitrogen into surfaces. Experimental setup diagram of the technique is given in Figure 2.2.

The technique basically relies on acceleration of ions by ion source to impact target material. The implantation phenomenon starts with the acceleration of ions and it is directed towards a substrate which is called “target” (316 SS in this case). The energy of the ions might be in the range of several kilo electronvolts to few mega electronvolt. These levels of energy could cause significant changes in the surface by the ions penetration (Izman, Shah, Nazim, Hassan, Anwar, Abdul-Kadir and Rosliza 2012). However, unless the energy of ions is selected carefully, the ions may penetrate deep

inside of the substrate, which is an undesirable case. Therefore, the surface modifications are limited to the near-surface region and a depth of 1 μm from the surface is normal (Rautray, Narayanan and Kim 2011). In other words, bulk material properties will not be affected by the ion implantation process.

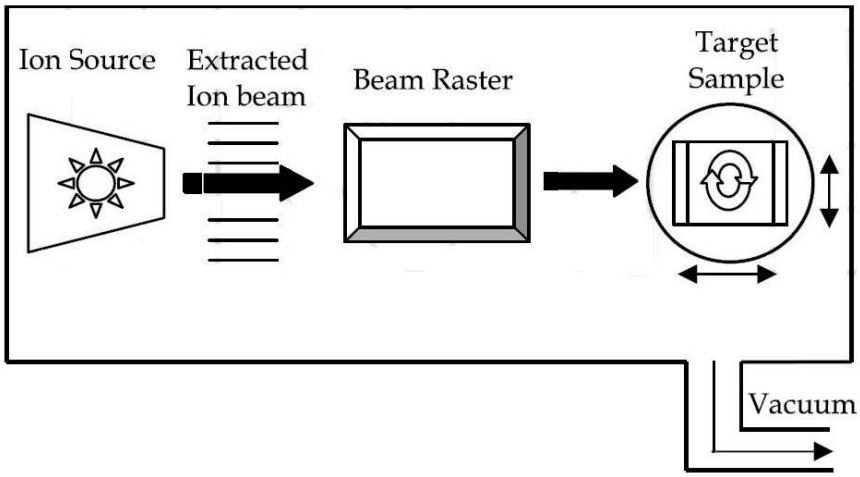

Figure 2.2. Schematic diagram of beam line ion implantation system
(Source: Izman et al., 2012)

A systematic series of 316 stainless steel samples has been prepared as a function of exposure time to a nitrogen ion beam in this study. Sample preparation mainly includes polishing, Ar-ion sputtering and nitrogen implantation steps. A series of 3 samples was prepared from AISI-316 stainless steel discs (3 cm diameter × 3 mm thickness) cut from commercial round stock in Colorado School of Mines. Although in the earlier research of D.L. Williomson et al.(Williamson, Wilbur, Fickett and Parascandola 2001), they used a relatively high energy beam (60 keV), it became clear with the enhanced diffusion at elevated temperatures that relatively low energies (~1 keV) were adequate, in other saying, the higher N content achievable with the reduced energies and higher beam fluxes result in clear observation of the magnetic state of γ_N by Mössbauer spectroscopy (Wei, Shogrin, Wilbur, Ozturk, Williamson, Ivanov and Metin 1994, Williamson, Ozturk, Wei and Wilbur 1994) confirming the early observation that the γ_N phase was ferromagnetic (Ichii, Fujimura and Takase 1986).

Before ion implantation, each disc was polished to a mirror-like finish, cleaned in chloretone and then acetone before being placed in the vacuum system for ion-beam processing. A pre-treatment, Ar-sputtering namely, was performed just before N ion implantation with the aim of removal of C contamination on the sample surfaces. Each

sample was sputter-cleaned for 10 minutes in an Ar-ion beam with other conditions maintained as follows: ion energy potential = 1 kV, current density = 2.5 mA/cm^2 during which time its temperature was raised to 410°C with the aid of a substrate heater. N-ion beam processing was performed following this step immediately. Ion implantation time ranges from 30 minutes to 240 minutes at relatively low energy (700 V), and high flux (2.0 mA cm^{-2}) conditions, with the sample maintained at 410 ± 20°C.

2.3. Experimental Methods

In this study, magnetic, compositional, structural and topographical features will be investigated by the following techniques;

- θ / 2θ X-Ray Diffraction (Bragg-Brentano)
- Grazing Incidence X-Ray Diffraction (GIXRD)
- Scanning Electron Microscopy (SEM)
- Energy Dispersive X-Ray Spectroscopy (EDS)
- Atomic Force Microscopy (AFM)
- Magnetic Force Microscopy (MFM)
- Vibrating Sample Magnetometer (VSM)
- Magneto-Optic Kerr Effect Spectroscopy (MOKE)

Each technique has different benefit in terms of its analytical function. With this approach, phase analysis and surface crystal structures have been investigated by X-ray diffraction in both θ/ 2θ geometry (XRD) and grazing incident (GIXRD) modes, surface topography has been studied by scanning electron microscopy (SEM) as well as atomic force microscopy (AFM) and elemental composition in phase has been estimated by energy dispersive x-ray spectroscopy (EDS) while magnetic features of N ion implanted layers have been characterized by magnetic force microscopy (MFM), magneto-optic Kerr effect (MOKE) and vibrating sample magnetometer (VSM).

2.3.1. X-Ray Diffraction Analysis

X-ray diffraction can be used for characterization of near surface layers since low energy X-rays are strongly absorbed in passing through the solid material. The fundamental physical and chemical knowledge obtained by this analysis may be classified as: chemical composition and crystal structure, layer composition and thickness determination. This method was used for determination of present expanded austenite phase on the surface of 316 SS in this study.

X-ray diffraction analysis (XRD) is a non-destructive technique for the identification of atomic structures of non-amorphous materials. Firstly X-rays were coincidentally discovered by Wilhelm Röntgen while he was working at the University Of Wurzburg, Germany in November 1895. They have been used for decades to study the structure of the bulk crystalline materials.

Practical use of X-ray diffraction in crystals was developed by W.H. Bragg and his son W.L. Bragg in Cambridge in around 1912. Basically, the information is obtained by the diffraction of X-rays by a crystalline material, which is a process of scattering of the beam by the electrons associated with the atoms in any crystal. Destructive and constructive interferences of these scattered X-rays due to periodic arrangement of the atoms in the crystal and its symmetry have main role for identification of materials by created different X-ray patterns for any individual material. On top of that X-rays have been mainly using to identify phases and compounds, by their investigation capabilities their functionality has showed wide range of use. They help researchers to give information about composition, phase transformation, texture, residual stresses in crystal lattices, refractive indices, roughness, and even layer thickness.

X-rays are generated by either X-ray tubes or synchrotron radiation. Primary X-ray source, called as X-ray tube consisting of a cathode ray tube with a heated filament, produces electrons. X-rays are generated when these electrons are accelerated and bombard a stationary or rotating metal target. This target metal is often made by copper, cobalt or molybdenum. As electrons collide with atoms in the target, continuous spectrum of X-rays is emitted and X-rays are created with characteristic wavelengths. These X-rays are emitted in all directions. The ones making an angle of 3^{o} to 6^{o} are convenient to pass through a window (made of low atomic number, low absorption

element: beryllium) and they are filtered to a single wavelength, collimated and directed to the sample. Figure 2.3 shows the components of X-ray tube.

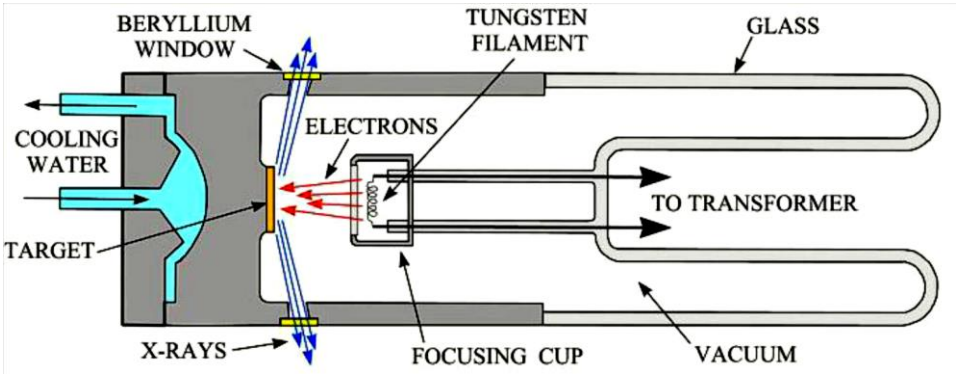

Figure 2.3. Schematic view of x-ray tube
(Source: Poppe, Paskevich, Hathaway and Blackwood 2001)

On the sample surface the incident X-rays are diffracted by suitably oriented crystallographic planes towards the detector which records and processes the signal. Geometrical considerations show that the scattering angles corresponding to diffracted intensity maxima can be described by **Bragg's equation**;

$$n\lambda = 2d_{hkl}\sin\theta \ (n = 1,2,3,..) \tag{2.1}$$

where d_{hkl}, λ, θ and n represent inter planar spacing from a set of hkl planes, wavelength of the X-rays, the angle of diffraction and the diffraction order, respectively.

Over few decades, numerous companies have built X-ray diffraction instruments in order to fulfill different kinds of X-ray diffraction tasks and obtain detailed data. Philips X'pert Pro MRD System Thin Film X-Ray Diffraction Equipment facilitated by Department of Physics of Izmir Institute of Technology was used to obtain phase information from the nitrogen ion implanted specimens. Figure 2.4 illustrates mentioned equipment and its parts. Analyzing crystal structure identification, lattice expansion, layer thickness and texture evolution was the main purpose of this characterization.

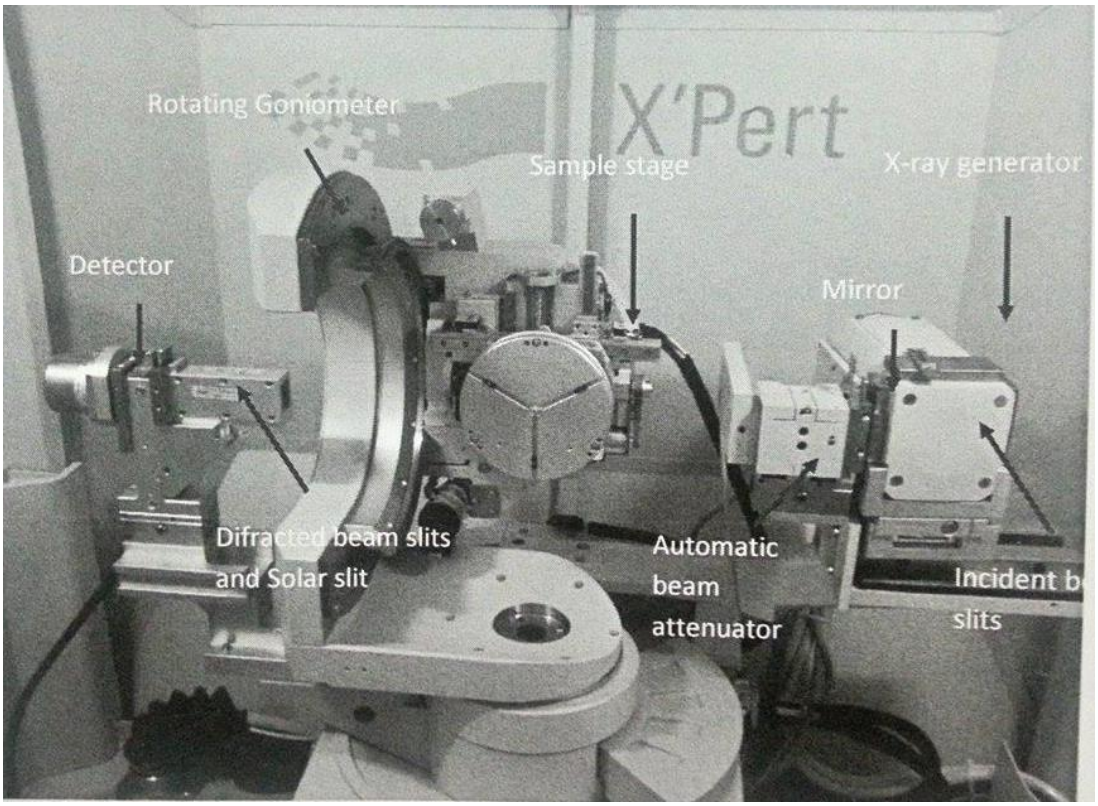

Figure 2.4. Thin Film Philips X'Pert Pro MRD System which was used for XRD experiments in this study, which is facilitated by Physics Department in Izmir Institute of Technology.

2.3.1.1. Bragg-Brentano Method

This method is known as θ/ 2θ XRD method as well. The schematic diagram is represented in Figure 2.5.

This method can be defined as a symmetric method since the system always detects the scattered X-rays at a diffraction angle which is equal to the angle of X-rays incident of the surface. Depending on the aim of the investigation and the properties of the sample, different experimental methods exist. For polycrystalline and powder samples the basic measurement geometry is the θ/ 2θ geometry where θ is the incident angle and 2θ the angle of the detector with respect to the incident beam. This means both the sample and the detector move step by step during the measurement and while the samples rotate at an angle (θ) the detector moves two times this angle (2θ). This method, therefore, always detects the diffracted X-rays from grains oriented parallel to the surfaces not the others. Additionally in the so-called Bragg-Brentano mode the X-ray source and the detector are always situated on the same circle. On the other hand,

the irradiated volume is the dominant effect at larger sample widths which favors Bragg-Brentano optics because of its wide, divergent X-ray beam. Bragg-Brentano case is rather superior for large samples. For this reason, the following method will be considered for near surface measurements.

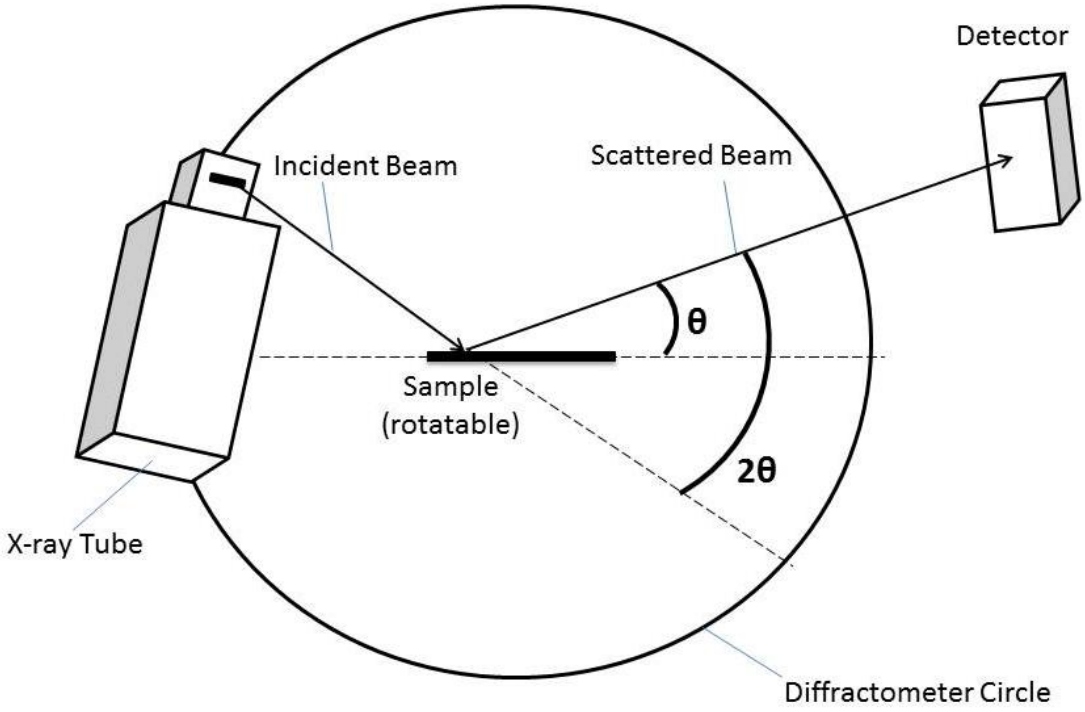

Figure 2.5. Geometry of an X-ray diffractometer in Bragg-Brentano geometry.

As can be seen from figure above, the sample surface is tangential to the focusing circle and the X-ray source and the detector are positioned on the diffractometer circle where it intersects the focusing circle. The reflections occur from planes set as at angle θ with respect to the incident beam and generates a reflected beam at an angle 2θ from the incident beam. The possible d-spacing defined by the indices (hkl) are determined by the shape of the unit cell.

When the scattered X-ray beams satisfy the Bragg's law in Equation 2.1, high intensity Bragg peaks are indicated in the diffraction pattern. Relying on Braggs's Law, accurate peak positions (2θ) from XRD pattern help to calculate lattice constant of cubic crystal structures from Equation 2.2;

$$d_{hkl} = \frac{a}{\sqrt{h^2 + k^2 + l^2}} \tag{2.2}$$

where a is lattice constant and h, k, l are miller indices of crystal.

One disadvantage of this geometry is that the effective depth probed by the incident beam always changes during the scan due to change in the angle of the incident beam. Due to change in the angle, the effective depth probed by the beam is increased depending on increasing incident beam angle. This case may sometimes cause some misinterpretation if it is not taken notice on examining for example, a material having layered-structure.

In our experiments, XRD measurements of nitrogen implanted samples were carried out by Cu-Kα_1 X-rays with wavelength (λ) of 1.5406 Å. The X-ray tube was fixed in this experiment while sample and detector were allowed to rotate along a goniometer circle on the sample-detector plane, the sample being at the center of the circle. The sample rotates to θ while the detector rotates to 2θ. The 2θ range for each specimen varies from 30^o to 100^o in 10 minutes duration, with a signal time of 0.5 s/ step. The scanning range was narrowed down to 35^o-55^o to focus on the peaks of interest. The data was collected with a computer-controlled system.

2.3.1.2. Grazing Incidence X-Ray Method

Grazing Incidence X-ray Diffraction (GIXRD) was utilized to obtain further information about near surface crystal structures on our nitrogen implanted samples.

Being different from the Bragg-Branteno method, GIXRD facilitates diffraction from the planes which are not parallel to the sample surface. The method uses very small incident angles and it is ideally suitable to provide information from quite thin layers. The main power behind this method involves providing the information layer by layer just changing the incident beam angle on the sample surface. Since the effective depth probed by the fixed X-ray beam incident on the sample is mainly dependent on the grazing angle (Cullity 1956). Another advantage of GIXRD is that the electric field at the critical angle is amplified locally by a factor of four, making the signal stronger (Als-Nielsen and McMorrow 2011)

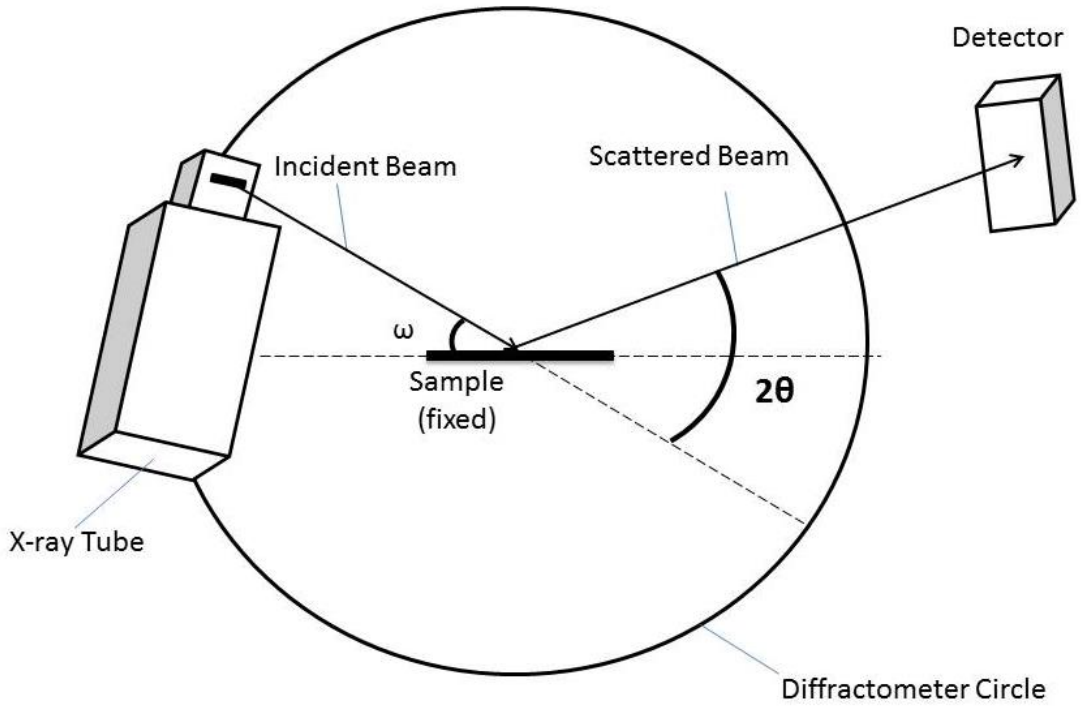

Figure 2.6. Geometry of an X-ray diffractometer in GIXRD mode

The near surface information from present phases in the layers was obtained by GIXRD. The measurements are performed at very low incident angles (ω) of 0.5^o,1^o, 2^o, 3^o, 4^o and 5^o to maximize the signal from the thin layers (50-100 nm) and to seek the texture evolution of peaks and peak shifts. Figure 2.6 represents the schematic diagram of GIXRD. The incident x-ray beam is fixed to a predetermined value on the sample and only the detector rotates 2θ degrees. The scanning angle (2θ) ranges between 35^o-55^o.

2.3.2. SEM Analysis

Scanning Electron Microscopy (SEM) was used to have 3D-view information of nitrogen implanted surface.

SEM enables to obtain topographical information such as surface features limited to a few nanometers, surface texture; morphological information such as shape, size and arrangement of detectable particles down to a few nanometers and compositional information in a 1 μm diameter such as elements contained the sample, mapping of elemental composition of a sample.

SEM is a type of technique to investigate and to visualize surface structures. In this technique electrons are used rather than light to form an image. When a finely focused electron beam with energy up to 30 keV strikes a sample, both photon and electron signals are emitted. These signals produced from interaction are collected by different detectors. Figure 2.7 illustrates these signals and the detectors collecting them.

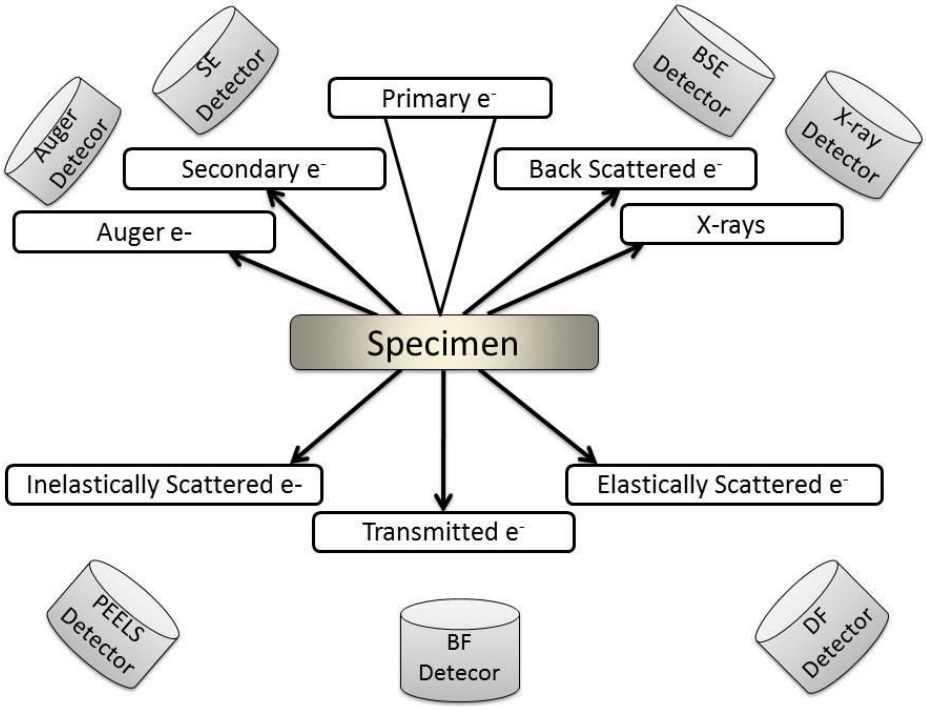

Figure 2.7. Detectors used in SEM

By means of their higher signal intensities, secondary electrons (SE), backscattered electrons (BSE), and characteristic X-rays are mainly used in SEM detectors, named as Secondary electrons (SE) detector, Back-Scattered Electrons (BSE) detector and Energy Dispersive X-ray detector, respectively. The signals produced corresponding to sample-electron interaction are simply shown in Figure 2.8.

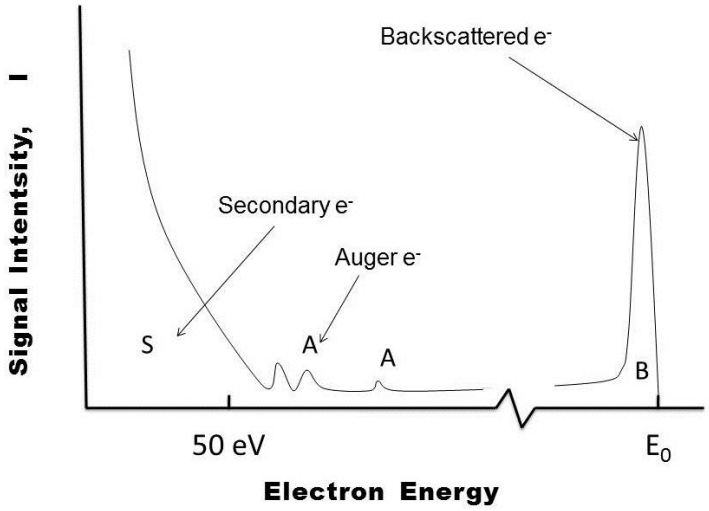

Figure 2.8. Signals produced of interaction between sample and electron beam

The most common imaging mode uses secondary electrons which are produced by inelastic scattering with beam electrons in the surface near regions down to about 50 nm. Since their yield depends strongly on the local surface inclination an excellent topography contrast can be achieved. Another mode, backscattered electron imaging, is based on elastic scattering interactions down to depth of 100 nm. They give information about the elemental distribution as the probability of backscattering depends on the atomic mass of the sample elements. Finally, the electron beam generates X-rays from the sample's atoms within a depth of one micrometer as well. The energy of each X-ray photon is characteristic of the elements which produced it. Thus, the so-called energy dispersive X-ray analysis (EDX) provides a further method for elemental identification. The resolution of SEM is essentially determined by the electron beam spot size which can be adjusted to values between 5 and 20 nm. Hence, a resolution limit down to a few nanometers can be achieved.

SEM micrographs used in this work were taken by a scanning electron microscope equipped with a Philips XL-305 FEG Scanning Electron Microscope in Materials Research Center at IYTE (IZTECH – MAM). The magnification of detectors ranges from 500x to 5000x while applied beam voltage is 20 keV for samples.

2.3.2.1. Energy Dispersive X-Ray Spectroscopy

Energy Dispersive X-ray mode was used to determine chemical compositions on the surfaces of nitrogen ion implanted 316 SS samples.

When the incident primary electron beams strike on the sample, the primary electron beams generate X-rays from the atoms of the sample as well as scattered electrons and backscattered electrons. These X-rays have a characteristic energy unique to the element which produced it and they can be used to provide quantitative information about the elements present at a selected region on the sample corresponding to their unique characteristics. The information is collected with energy-dispersive X-ray (EDX) detector in SEM within a depth about 1-3 μm.

In this study, randomly selected regions in different sizes revealed the elemental distribution on the layers. Additionally, an average N concentration was estimated by EDX measurements which were taken on at least five different regions of the N implanted surfaces.

2.3.3. Roughness Measurements

Roughness measurements were performed on the surfaces of nitrogen ion implanted 316 SS samples by using Atomic Force Microscopy (AFM) tapping mode. During low energy, high-flux nitrogen implantation process samples are subjected to detrimental sputtering resulting in change in surface quality. The aim of these measurements was to have information of this change in surface quality due to the processing time. The roughness values were measured for each sample that are subjected to different process durations (30 minutes, 90 minutes, 240 minutes). In pursuit of roughness profiles from different scales and different regions of samples were collected, roughness values were calculated for each. Average roughness value (R_a) as well as root mean square (R_q) for each sample was calculated and how process duration affects the roughness was discussed by interpreting them.

2.3.3.1. Atomic Force Microscopy

Atomic Force Microscopy (AFM), in this study, was used to investigate surface morphology and surface rougness of nitrogen ion implanted SS specimens.

AFM provides a 3D profile of the surface at nanoscale, by measuring forces between a sharp tip (probe) (<10 nm) and surface at very short distance (0.2-10 nm probe-sample distance). The components of AFM system are represented in Figure 2.9. As can be seen, a tip radius of curvature is supported at the end of a flexible cantilever. This tip "gently" touches the sample surface and records the small forces (mechanical contact force, van der Waals forces, capillary forces, chemical bonding, electrostatic forces, magnetic forces, solvation forces etc) between the tip and the surface to scan the specimen surface. Along with force, additional quantities may simultaneously be measured through the use of specialized types of probes. The cantilever is typically made by silicon (Si) or silicon nitride (Si_3N_4). Measuring cantilever deflection enables to evaluate the tip – surface interactive force.

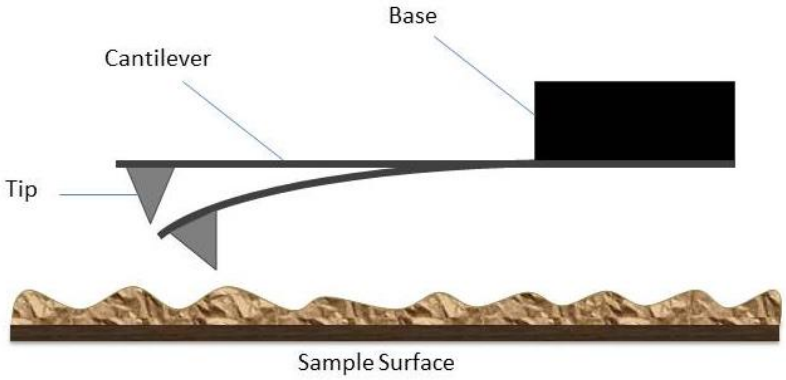

Figure 2.9. A schematic view of AFM tip cantilever

In this study, AFM measurements were performed in semi-contact (tapping) mode with the help of a commercial AFM system (Digital Instruments-MMSPM Nanoscope IV) facilitated in Research Center of Materials of IYTE (IZTECH – MAM). Size of the scanning area of the samples was 50 μm x 50 μm.

2.3.4. Magnetic Characterization

Magnetic characterization is the main focus point of this study. In order to understand the effect of implantation time on the magnetic characteristics of expanded austenite phase, γ_N, the following characterization methods were performed: i) Magnetic Force Microscopy (MFM), Magneto-Optical Kerr Effect (MOKE) analysis, Vibrating Sample Magnetometer (VSM) on the samples.

2.3.4.1. Magnetic Force Microscopy

Magnetic Force Microscopy (MFM) is one of the modes of Scanning Probe Microscopy. In this study, MFM was used to investigate magnetic properties of the N implanted surfaces. In this mode, the probe is coated with a ferromagnetic film (eg. CoCr or FeNi) to give an image showing the variation of magnetic force between the magnetized probe and magnetic stray field from N implanted layers.

In MFM measurements, topographical image and magnetic data can be simultaneously measured via the two-pass technique. In this technique, first pass in semi-contact (tapping) mode is a standard mode of AFM trace. The tip maps out the surface topography the surface topography along surface. Later, in the second pass (lift mode), the magnetic probe tip traces the sample surface at an above height (range between 30-300 nm) one more time. The aim of this tracing is to minimize the effect of Van der Waals bound forces. In the lift mode, the tip is more sensitive to far field magnetic force than short range Van Der Waals forces. (Wozniak, Glowacka and Kozubowski 2005). An earlier study shows that (Neves and Andrade 1999) the magnetic interactions occur between 5 and 300 nm in stainless steels. During the lift mode, the tip scans the same path of tapping mode. After as far as the influence of Van der Waals forces are eliminated, influence of magnetic interactions between the magnetically coated tip and the magnetic sample is monitored by observing changes in resonance frequency of the tip. As a result of combination of those two modes, topographical images and magnetic data can be obtained by laser/photo-detector.

The magnetic interaction force, F, between the ferromagnetic tip and the stray field emanating from the sample surface is related to magnetic moment and magnetic field. Equation 2.3 shows the relation between them;

$$\vec{F} = (\vec{m}\vec{\nabla})\vec{H}_s \tag{2.3}$$

where m stands for the magnetic moment of the tip and H_s is the magnetic stray field of the sample.

Magnetic domains of surfaces were imaged by Veeco, Dimension 3100 and CoCr coated tip coated tip with radius of 40 nm and frequency of 60-100 kHz was used. Lift height is fixed between the range of 60-300 nm. The samples were cut into smaller pieces of 1cm x 1 cm before the measurements.

2.3.4.2. Vibrating Sample Magnetometer

Vibrating sample magnetometer (VSM) was used to obtain hysteresis curves of the nitrogen ion implanted samples.

VSM is a technique which measures the magnetic moment of a sample when it is vibrated perpendicularly to a uniform magnetizing field. The instrumentation was first invented by Simon Foner in 1955 (Foner 1959). The technique is based on Faraday's Law of Induction, which states that a changing magnetic field will produce an electric field. This electric field can be measured and can tell us information about the changing magnetic field.

The working principle of the technique will be explained after explanation of a few concepts of magnetism. These concepts lead to understanding of magnetic properties of the studied samples as well as interpret the results of magnetic characterization analyses (VSM and MOKE).

The **magnetic induction**, or **magnetic flux density**, denoted by **B**, represents the magnitude of the internal field strength within a substance that is subjected to an H field. Both B and H are field vectors; hence, they are not only characterized by magnitude, but also by direction in space.

The magnetic field strength and flux density are related according to the Equation 2.4;

$$\vec{B} = \mu\vec{H} \tag{2.4}$$

The parameter μ is called the **permeability**, which is a property of the specific medium through which the H field passes and in which B is measured. The permeability

has dimensions of webers per ampere-meter (Wb/ A-m) and henries per meter (H/ m) (Callister and Rethwisch 2012).

In free space (vacuum), since there is no magnetization, the magnetic field is described by the vector fields B and H which are linearly related by;

$$\vec{B} = \mu_0 \vec{H} \tag{2.5}$$

where μ_0 is the permeability of free space ($\mu_0 = 4\pi \times 10^{-7}$ H/m).

However, in a magnetic solid the relation between B and H is more complicated. Both two vector fields may be in very different directions and magnitudes. Thus, there comes a new quantity, **M**, called the **magnetization** of the solid, is defined by the expression;

$$\vec{B} = \mu_0 \vec{H} + \mu_0 \vec{M} = \mu_0 (\vec{H} + \vec{M}) \tag{2.6}$$

For a diamagnetic or paramagnetic material, the magnitude of M is proportional to the applied field as follows,

$$\vec{M} = \chi \vec{H} \tag{2.7}$$

where χ is a dimensionless quantity, called **magnetic susceptibility.** The solid is called a **linear material**.

In other case, for ferromagnetic materials, there is still linear relationship between B and H, namely,

$$\vec{B} = \mu_0 (1 + \chi) \vec{H} = \mu_0 \mu_r \vec{H} \tag{2.8}$$

where $\mu_r = 1 + \chi$ is the relative permeability.

In this study, the unit (dimension) of magnetization was taken as **emu** while dimension of magnetic flux density was taken as **gauss.** (1 Wb / m2 = 104 gauss) and magnetic field strength was taken as **oersted.**

All materials can be classified in terms of their magnetic behavior depending on their bulk **magnetic susceptibility**, χ and **permeability, μ.** The general classification of materials according to their magnetic properties can be listed in Table 2.3.

Table 2.3. Classification materials due to their magnetic properties

$\mu < 1$	$\chi < 0$	**diamagnetic**
$\mu > 1$	$\chi > 0$	**paramagnetic**
$\mu >> 1$	$\chi >> 0$	**ferromagnetic**

In addition to these, magnetic nature of materials shows characteristic variations of the magnetic susceptibility with temperature. As can be seen from Figure 2.10, in the case of ferromagnetism, above a certain point called "**Curie point**" the material displays a behavior similar to paramagnetic materials and when going under the Curie point the material displays strong magnetic properties, the material remains permanently spin aligned even when the field is removed. Ferromagnetism is commonly found in compounds containing iron and in alloys. On the other side, for paramagnetic materials there is no change in the magnetic susceptibility with temperature behavior at a specific point, and for diamagnets magnetic susceptibility remains fixed as the temperature increases.

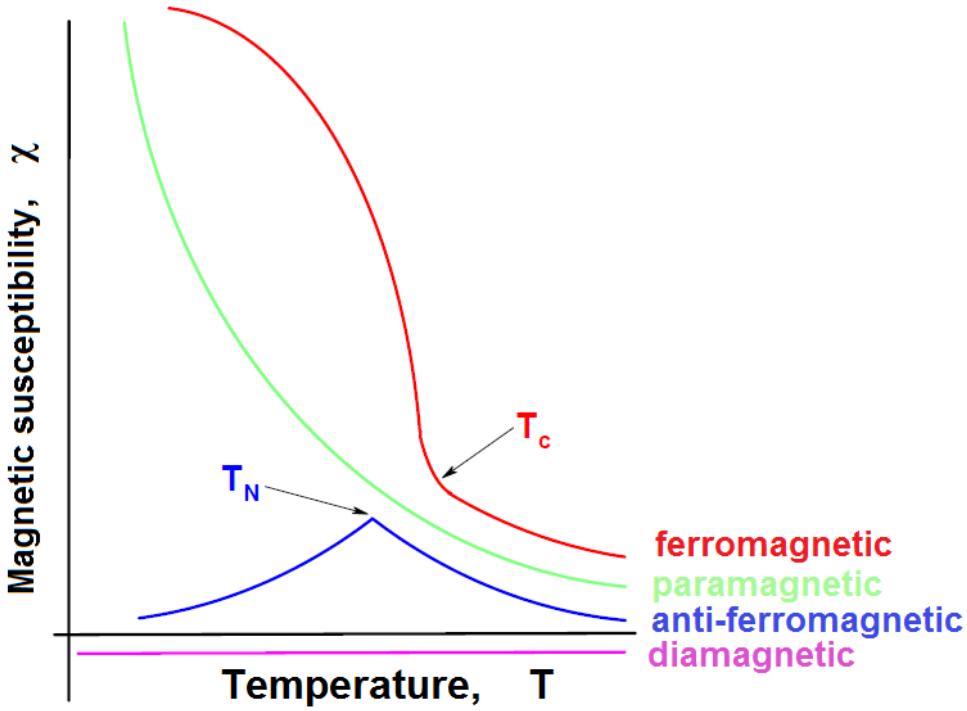

Figure 2.10. Magnetic susceptibility – Temperature relationship of materials (Source: Atkins 2010)

Diamagnetic materials are more likely to be water or water based materials with susceptibility, χ, is approximately -10^{-5}. For most paramagnetic materials χ has a range between 10^{-5} and 10^{-3}. Susceptibility varies from several hundred for steels to thousands of soft magnetic materials (Permalloys).

In our study, expanded austenite phase is found to have ferromagnetic as well as paramagnetic characteristics. In order to describe them as paramagnetic or ferromagnetic, their hysteresis loops should be investigated.

Magnetic materials are differentiated by their behavior in external magnetic fields. Ferromagnetic materials exhibit a history-dependent behavior called “hysteresis”. Hysteresis behavior and permanent magnetization may be explained by the motion of domain walls (Callister and Rethwisch 2012). When a material is located under a continuous current (created by a coil), initially large numbers of domains align with the externally applied field as the the current in the coil is increased. A torque move occurs on the dipoles of unaligned domain.

Figure 2.11 represents a typical ferromagnetic hysteresis loop and indicates the predominant, underlying mechanisms for each region the hysteresis loop of a ferromagnetic material.

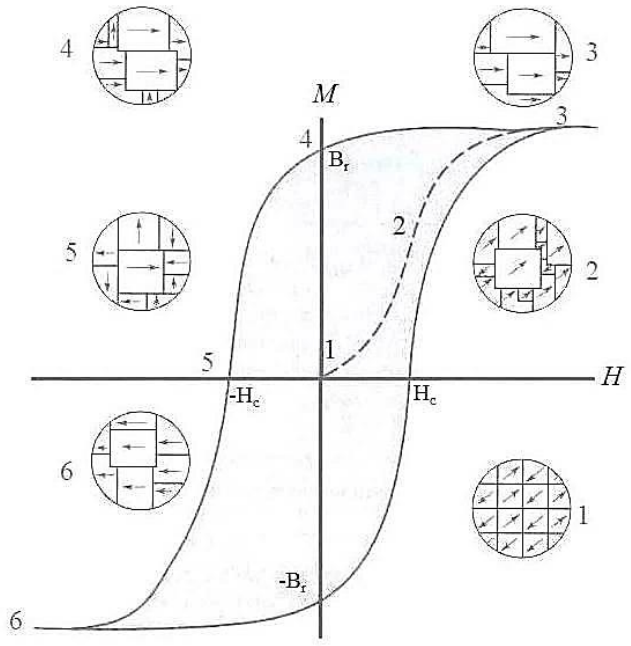

Figure 2.11. Hysteresis loop of a ferromagnetic material with virgin curve also shown (1-2-3)

Once most domains are aligned there can be little further increase in M, this is called saturation. If the current is now wound back to zero, the magnetization does not follow the original curve, it lags behind: this is called as hysteresis.

First, the sample is magnetized to saturation in an applied field (virgin curve). The region of highest permeability is governed by domain wall motion, whereas magnetization rotation occurs at higher magnetic fields. When the applied field is reduced to zero, the remanent magnetization M_r remains. A magnetic field of opposite direction, called the coercivity field H_c, is needed to macroscopically demagnetize the sample.

- At point 1: initial magnetization
- At point 2: domains line up with applied field.
- At point 3: little further alignment with increasing field due to saturation
- 3 - 4: demagnetization but $M \neq 0$ again when $H = 0$ again
- 4 - 5: current direction reversed, $M \neq 0$ at 5
- 5 - 6: saturation with all dipoles in reverse direction
- At Br and -Br there is a permanent magnetization even with $H = 0$

As it is mentioned earlier, the hysteresis loop contains important information about the magnetic properties of the sample. Characteristic quantities include the saturation magnetization M_s, the remanent magnetization M_r, the coercivity field H_c, permeability μ and the dissipated energy that is necessary to magnetize the sample in the opposite direction. The dissipated energy can be calculated from the area that is inside the hysteresis loop.

Setup of VSM allows exploration of a common experimental technique for measuring magnetic material properties such as hysteresis, saturation, coercivity, and anisotropy. The operation of the VSM is fairly simple. (Figure 2.12) A magnetic sample is placed on a long rod and then driven by a mechanical vibrator. The rod is positioned between the pole pieces of an electromagnet, to which detection coils have been mounted. The oscillatory motion of the magnetized sample will induce a voltage in the detection coils. The induced voltage is proportional to the sample's magnetization, which can be varied by changing the dc magnetic field produced by the electromagnet (Burgei, Pechan and Jaeger 2003).

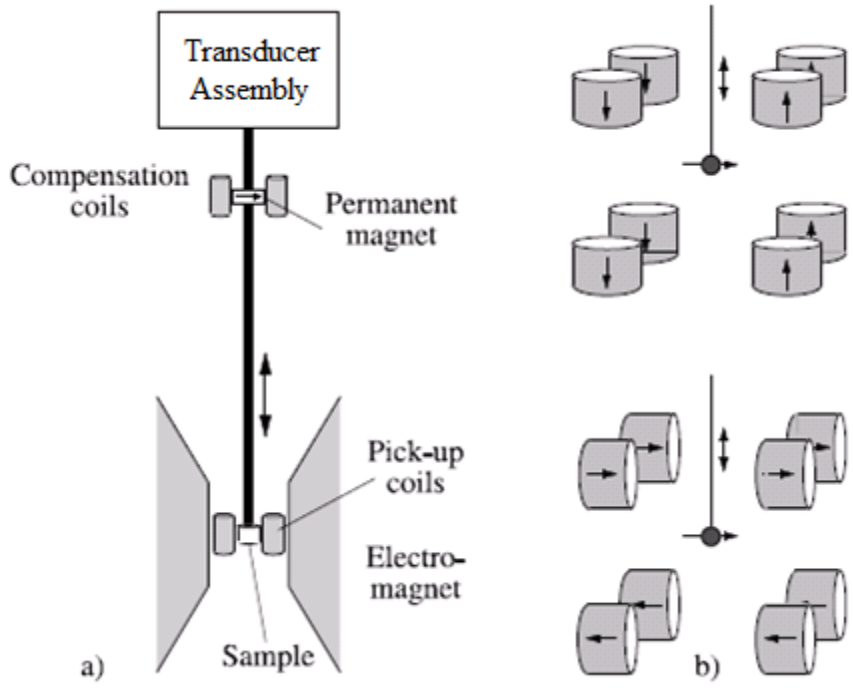

Figure 2.12. Schematic representation of a vibrating sample magnetometer

There is an essential point to be mentioned for magnetic measurement analyses. The energy required to magnetize a crystal in a ferromagnetic material depends on the direction of the applied field relative to the crystal axes. If the magnetic properties of a sample are dependent on direction, it is magnetically anisotropic. Magnetic anisotropy arises from dipole-dipole interactions and spin-orbit coupling. From the technological viewpoint this magnetic anisotropy is one of the most important properties of magnetic materials (Johnson, Bloemen, Den Broeder and De Vries 1996).

Another form of magnetic anisotropy is the magnetocrystalline anisotropy. When investigating single crystalline Fe, Ni or Co samples, one notices that the magnetization curves along certain crystallographic directions differ from each other. In iron, the magnetization curve along the [100] direction is steeper and reaches saturation at lower external fields than along [110] or [111], and is therefore called the easy axis of magnetization. In case of nickel, [111] is the easy axis and [100] the hard axis of magnetization. In the absence of an external field, the spontaneous magnetization lies preferably along one of the easy axes. The origin of the magnetocrystalline anisotropy lies both in the coupling of the spin part of the magnetic moment to the electronic orbital shape and orientation (spin-orbit coupling) and the chemical bonding of the

orbitals on a given atom in their local environment (Johnson, Bloemen, Den Broeder and De Vries 1996).

From this technical view, the change in the direction of the magnetic field to the layer makes two different anisotropy, in-plane magnetization and out-of plane magnetization. In-plane magnetization stands for magnetic field axis is parallel to sample while out-of-plane magnetization geometry stands for magnetic field axis is perpendicular to sample.

In both VSM and MOKE measurements, magnetic fields both parallel (in-plane) and perpendicular (out-of-plane) to the samples were applied to nitrogen ion implanted samples. The differences between two kinds of data have been discussed. VSM measurements in this study were performed in Department of Physics at Izmir Institute of Technology.

2.3.4.3. Magneto-Optical Kerr Effect

In this study, Magneto-optic Kerr Effect (MOKE) analysis was used to obtain the hysteresis loops of the nitrogen implanted 316 SS samples.

The term "magneto-optical" was first called by Michael Faraday in 1845. He observed a rotation of polarized light transmitted of a glass material depending on the magnitude of an axial magnetic field. When he tries to carry out the same experiment on light reflecting metallic material, surface defects could not enable to have fine results. Later than him, in 1877, John Kerr observed a rotation of the polarization of light reflected from a ferromagnetic. The Faraday and Kerr magneto-optical effects manifests themselves in a rotation of the polarization of the incident light and in a change in the polarization of the reflected light upon interaction with a magnetic material.

MOKE is a simple and straightforward optical method for magnetically characterization of magnetic materials. Visible, linearly polarized light is reflected from sample surface. The instrumentation of MOKE including small rotations in the polarization and small changes in the ellipticity of the light are represented. These optical effects result from the interaction of the incident light with the conduction electrons in the magnetic solid. The magnitude of the rotation of the polarization is directly proportional to the net magnetization (M) of the material reflecting the light. (Figure 2.13)

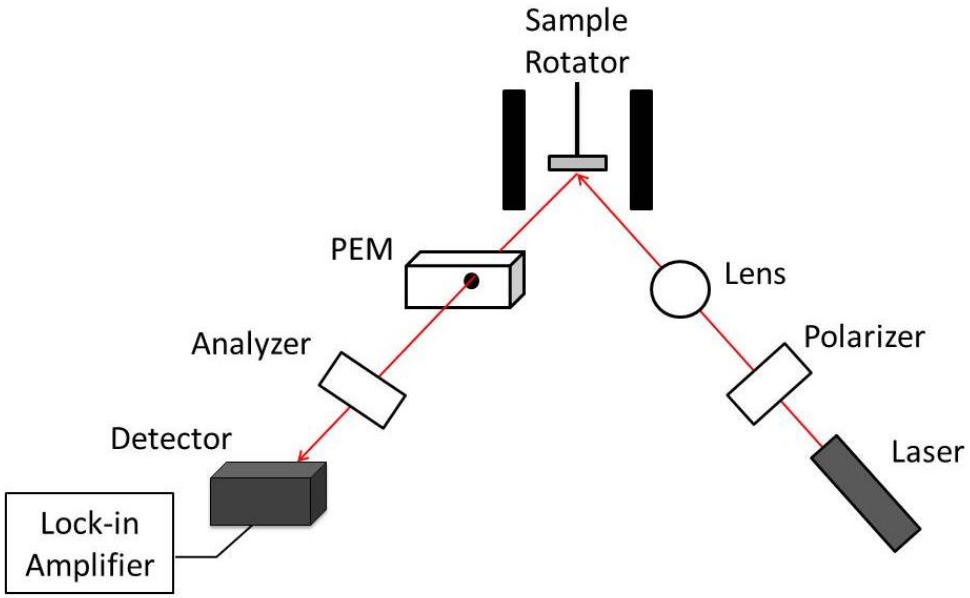

Figure 2.13. Schematic diagram of MOKE setup

Since MOKE is an optical probe, its lateral resolution is governed by the diffraction limit of the light source, range between 0.3 μm – 0.5 μm for typical wavelengths. Its probing depth is determining by the formula below;

$$I/I_0 = \exp(-t/\lambda) \tag{2.9}$$

where the reflected light intensity from a given depth I_0 is reduced to I for an optical path length, t, from the surface due to light absorption in the medium, absorption is scaled by a characteristic reduction length called the optical skin depth λ. For metals, as the materials of this study, λ is on the order of 10 – 20 nm at visible frequencies. As a consequence, of the fairly long probing depth of MOKE at optical wavelengths, it is used to analyze ferromagnetic layers buried by 10 nm or so of an absorbing, non-magnetic layer. When the magnetic layer thickness d >> λ the technique is generally refer to as MOKE, whereas d << λ SMOKE (Surface MOKE) is sometimes used.

In this study, nitrogen ion implanted layers of 316 stainless steel specimens were examined in MOKE. However, since 316 SS specimens do not have a smooth surface, the laser of MOKE was not able to collect signals from two of them. As an example, a 304 SS well-polished sample without ion implantation was examined. A clear hysteresis loop data can be seen in Figure 2.14.

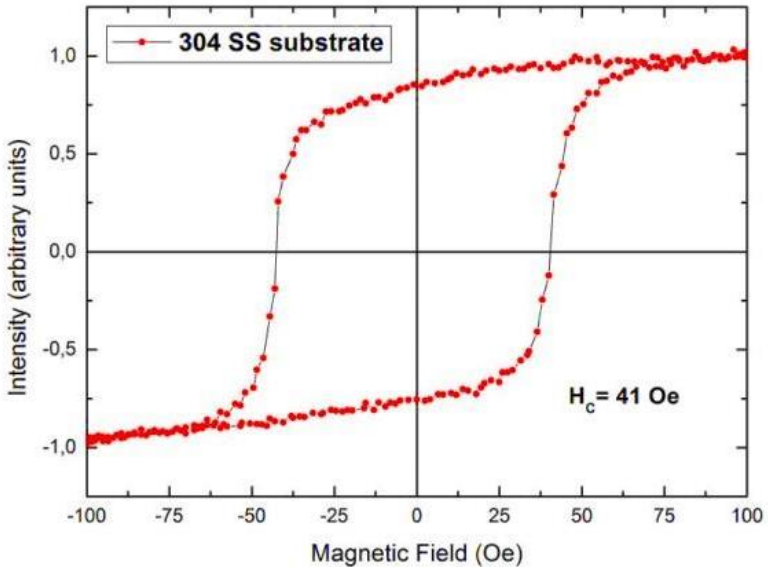

Figure 2.14. MOKE data of 304 SS substrate specimen

304 SS is typically nonmagnetic at ambient conditions (paramagnetic). As a result of polishing, the fcc crystal structure of specimen transforms to bcc or bct structure. This phase transformation caused by mechanical force is called as strain induced martensite. Thickness of the layer has been estimated approximately to be 50-100 nm thick. As can be seen from the results 304 SS substrate demonstrates ferromagnetic type behavior.

MOKE experiment was performed in the Department of Physics at Gebze Institute of Technology.

CHAPTER 3

RESULTS AND DISCUSSIONS

3.1. Microstructural Characterization and Phase Formation

Insertion of additional atoms into substrate is strongly correlated with the crystal lattice of the host material, thus, investigation of phase formation after N insertion is essential. In this following chapter, phase formation of austenitic stainless steel after low-energy high-flux conventional ion beam line ion implantation will be studied.

This part presents the formation of expanded austenite at different processing time conditions due to lattice expansions and the dependency of the lattice parameter on the nitrogen content. The nitrogen implanted layer phases were investigated with X-ray diffraction (XRD) in both symmetric θ/2θ and grazing-incidence (GIXRD) modes.

3.1.1. Results of XRD Analysis

XRD analysis was carried out on nitrogen implanted 316 SS samples as well as substrate due to different processing time ranging from 30 to 240 minutes. The angle formed between the tube and the detector, 2θ ranges from 35° and 55° in the analyses. This scanning range enables to observe (111) and (200) peaks, that are most outstanding ones compared to the higher (hkl) data range.

To understand better the phase distribution with depth in the N implanted layers, grazing incidence X-ray diffraction (GIXRD) of the N implanted samples was carried out at the incident angles of ω = 0.5, 1, 2, 3, 4 and 5 degrees, respectively. GIXRD analysis was also performed in 2θ between 35°-55° region.

3.1.1.1. Bragg-Brentano (θ/2θ) Configuration

In Figure 3.1 the X-ray diffraction patterns of nitrogen ion implanted 316 stainless steel after different process times are presented. The substrate material has a

predominantly fcc lattice structure [i.e., fcc γ] In this figure, the fcc substrate peaks are labeled as γ (hkl) and the nitrogen implanted ones as γ_N (hkl). Analyzing the XRD data, one can see that formation of expanded austenite phase, γ_N, present for all processing times. The results clearly indicate that the nitrogen implanted layer is composed of the high-N content phase γ_N. The γ_N formation is consistent with previous studies, where it was always observed when the substrate temperature was held near 400 ^oC. The XRD results for the nitrided sample are consistent with those of other low-pressure plasma nitrogen implanted and low-energy, high-flux N implanted SS samples, in that the γ_N (200) peak is shifted more than the γ_N (111) relative to the substrate peaks (Jiang and Meletis 2000, Abrasonis, Rivière, Templier, Pranevičius and Barradas 2005).

In Table 3.1, it can be clearly seen that N content is larger for each processing time in the (200) oriented grains. The narrow and symmetric nature of the γ_N peaks in Figure 3.1 suggest a uniform nitrogen distribution in the nitrogen implanted layer (Öztürk, Okur and Riviere 2009). The results suggest a correlation between phase formation and nitrogen insertion, where increasing layer thickness with increasing processing time was observed. (200) γ_N peak is shifted more than (111) γ_N peak suggesting grain-dependent N content behavior.

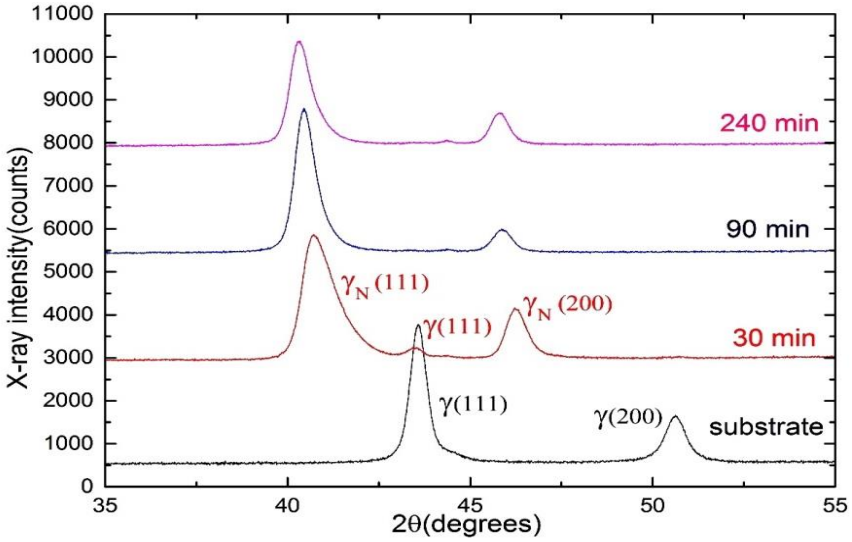

Figure 3.1. XRD data for the nitrogen implanted 316L specimens as a function of different implantation times and also 316L SS substrate alloy

Table 3.1. Lattice parameters, d and a, 2θ for the 316L SS fcc substrate and fcc γ_N phases. Δa/a refers to the relative difference in lattice spacing.

Implantation time (min.)	phase	2θ (degrees)	d (Å)	Lattice constant a (Å)	<a> (Å)	Lattice expansion Δa/a (%)
Substrate	γ_{111}	43,583	2,075	3,59		
	γ_{200}	50,623	1,802	3,60	3,60	-
30	γ_{N111}	40,816	1,960	3,83		6,7
	γ_{N200}	46,274	2,080	3,92	3,87	8.9
90	γ_{N111}	40,484	2,226	3,86		7,5
	γ_{N200}	45,876	1,977	3,95	3,90	9,7
240	γ_{N111}	40,360	2,233	3,87		7,8
	γ_{N200}	45,807	1,979	3,96	3,91	10

3.1.1.2. Grazing Incidence X-Ray Configuration

To reveal the N implanted layer phases at the very surface, grazing incidence x-ray diffraction (GIXRD) of the specimens. The GIXRD spectrums for 30-minutes N implanted 316 SS sample at various angles (ω = 0.5º, 1º, 2º, 3º, 4º, 5º) is shown in Figure 3.2. The GIXRD data showed the formation of expanded austenite phase, γ_N in the implanted layer.

Figure 3.3 represents that the GIXRD results for increasing incident angles indicate more and more contribution coming from the substrate phase and also increasing γ_N phase.

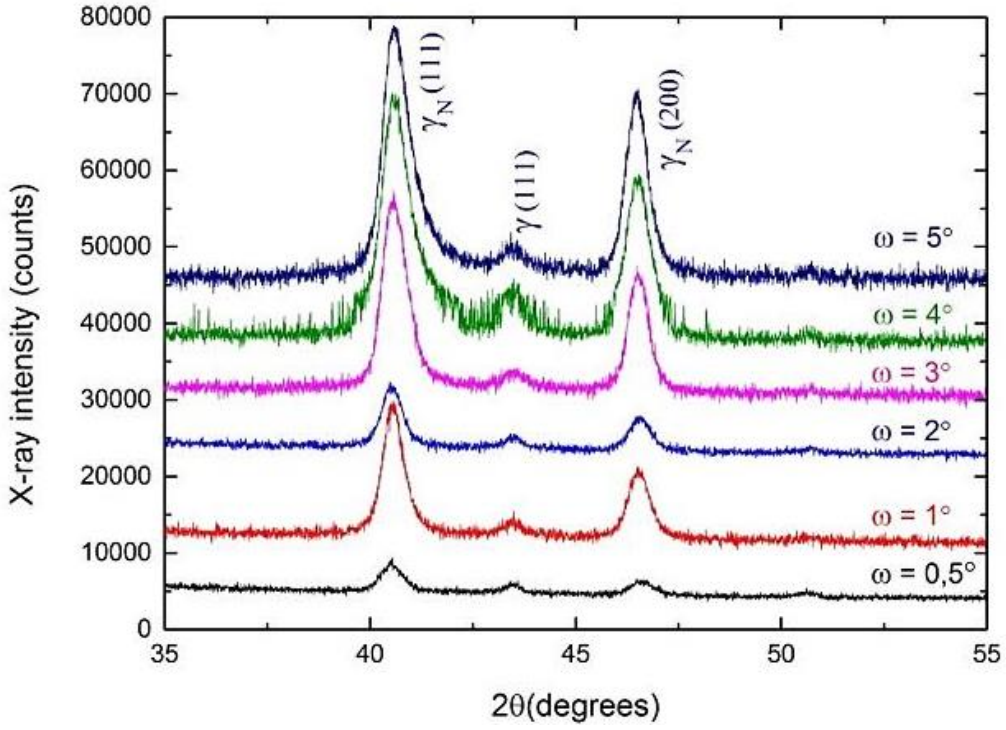

Figure 3.2. GIXRD results for 30-minutes N implanted 316 SS at different grazing angles from 0.5 to 5 degrees

(a) ω= 0,5º (b) ω= 1º

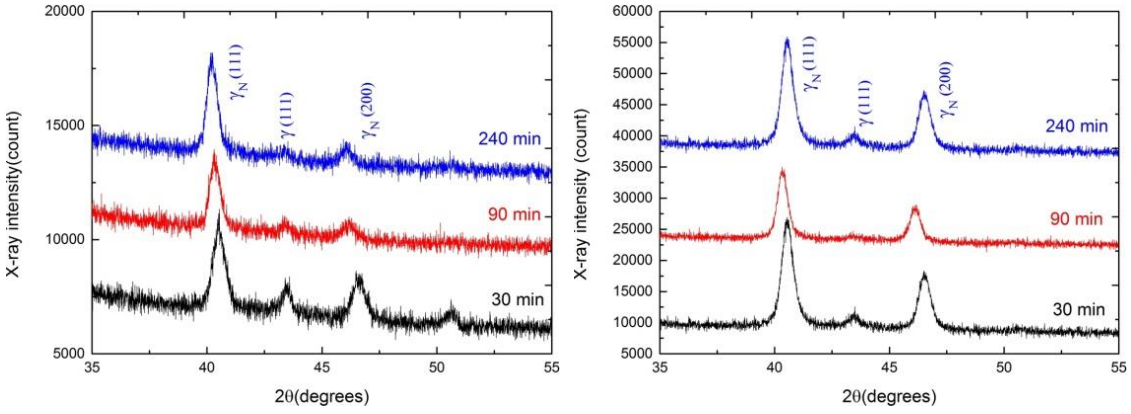

Figure 3.3.GIXRD results for all specimens at (a) ω = 0.5º, (b) ω = 1º, (c) ω = 2º, (d) ω = 3º, (e) ω = 4º and (f) ω = 5º

(Cont. on next page)

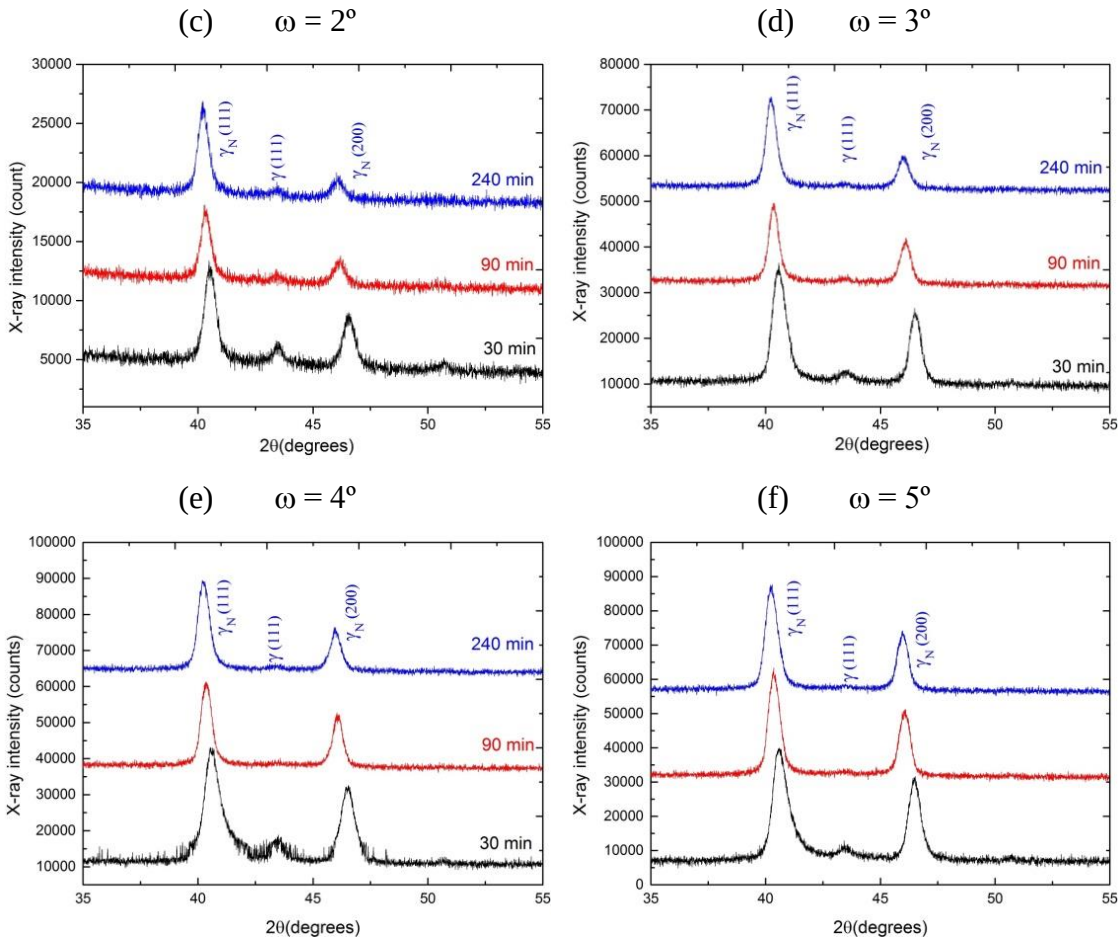

Figure 3.3. (Cont.)

3.2. Topographical Analysis

3.2.1. SEM Analysis Results and Discussions

SEM analysis was performed on the surface of N implanted specimens with different implantation times of 30, 90 and 240 minutes. Figure 3.4 reveals the topographical SEM results for the nitrogen implanted 316L SS specimens at different processing times. These images were taken sequentially over a span of several grains to look for N implanted surfaces. The magnification under working was changed for the each specimen on this purpose. (2500x for 30-mins N implanted layers, 2000x for both 90-mins and 240-mins N implanted layers.) The average nitrogen amount for the grains will be explained in the next section.

Figure 3.4 shows the change in surface morphology induced by the nitrogen implantation. In the images a very fine and homogenous grain structure of surfaces is clearly seen. The images clearly reveal the grain structure of the N implanted layers (fcc γ). Periodic arrays of lines on the nitrogen implanted surface indicating the presence of slip bands inside the grains can also be seen evidently. It can be interpreted that these slip bands can be sourced by strain resulting high nitrogen contents in the γ_N layer. The formation of slip bands suggests plastic deformation of the grains, and this, in turn, implies important compressive stresses operating in the γ_N layer. Thus, lattice expansion (nearly 7% and 9% for (111) and (200) planes, respectively; as indicated on the previous chapter) of a surface layer in coherence (lattice registry) with a substrate of the same fcc structure must provide a strong driving force for the plasticity observed in the γ_N layer.

The impact of low-energy, high-current density, nitrogen ion beams and plasmas on the mechanical and electrochemical properties of stainless steel is well established and they exist several publications (Collins, Hutchings, Short, Tendys, Li and Samandi 1995, Chen, Li, Bell and Dong 2008). Due to this fact, as the processing time increases this impact becomes more visible. Much more clear explanation can be presented when combining these 2D SEM images with 3D AFM images. Roughness measurements due to processing time will be discussed in Chapter 3.4. As also can be seen from the 2D images in the mentioned chapter, there is a deformation on the surfaces of specimens as the process time increases. Hence, this brings out that nitrogen implantation by means of high-flux ion bombardment has significant detrimental effect on the roughness for the polycrystalline material.

Another observation from the images in Figure 3.4 is that the grain size due to processing time remains unaltered.

(a) 30 minutes (b) 90 minutes (c) 240 minutes

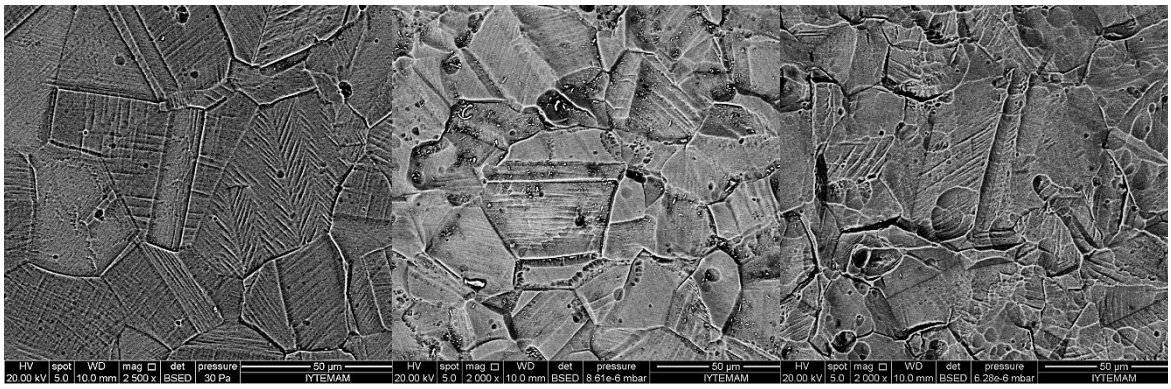

Figure 3.4. Topographical SEM images of (a) 30 minutes nitrogen ion implanted, (b) 90 minutes nitrogen ion implanted, (c) 240 minutes nitrogen ion implanted specimens.

3.3. Chemical Analysis

Elemental compositions of the nitrogen implanted 316 SS specimens at different processing times were investigated by EDX. Table 3.2 represents the average content of nitrogen on nitrogen implanted layers in both atomic and weight percent.

Table 3.2. Average N content in N ion implanted layers of 316 SS specimens

Implantation Time (minutes)	**N content (at.%)**	**N content (wt.%)**
30 minutes	27,75	10,2
90 minutes	27,03	10,2
240 minutes	29,31	10,6

Elemental compositions did not show any specific change due to processing time. The average nitrogen concentration of the N implanted layers with respect to different implantation temperatures changes between 27,75 at.% and 29,31 at.%. These findings of N concentrations are near to EPMA results of an earlier study (Öztürk and Williamson 1995). Note that since EDX is a semi-quantitative method, it is not capable of providing precise concentration of elements.

During nitrogen implantation, the nitrogen locates octahedral sites in the crystal structure of substrates by decreasing the atomic weight concentration of the base atoms (Fe, Cr, Ni) in the lattice.

3.4. Roughness Measurements

The images in Figure 3.5, Figure 3.6 and Figure 3.7 were obtained by AFM under the scanning area of 50x50 μm^2 scale. The average roughness (Ra) and RMS (root-mean-square) roughness values for each specimen were estimated based on at least three different scanning areas, 30x30 μm^2, 50x50 μm^2 and 100x100 μm^2.

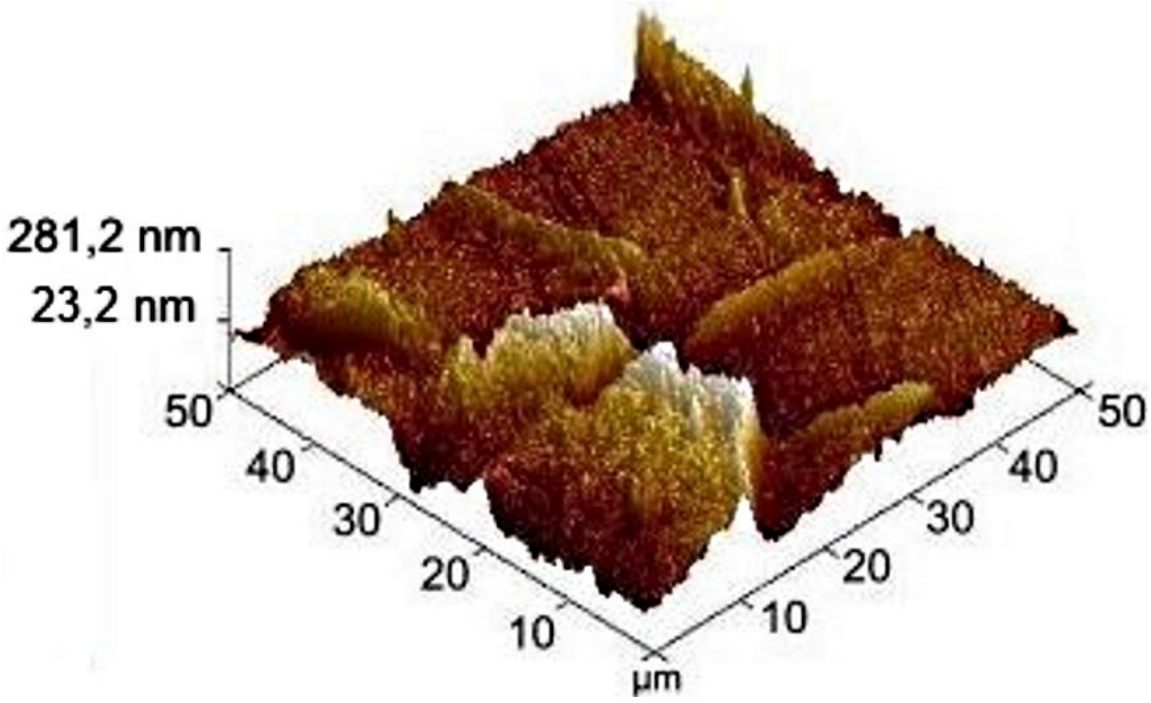

Figure 3.5. 3D image of nitrogen implanted 316 SS by AFM as a function of 30 minutes time

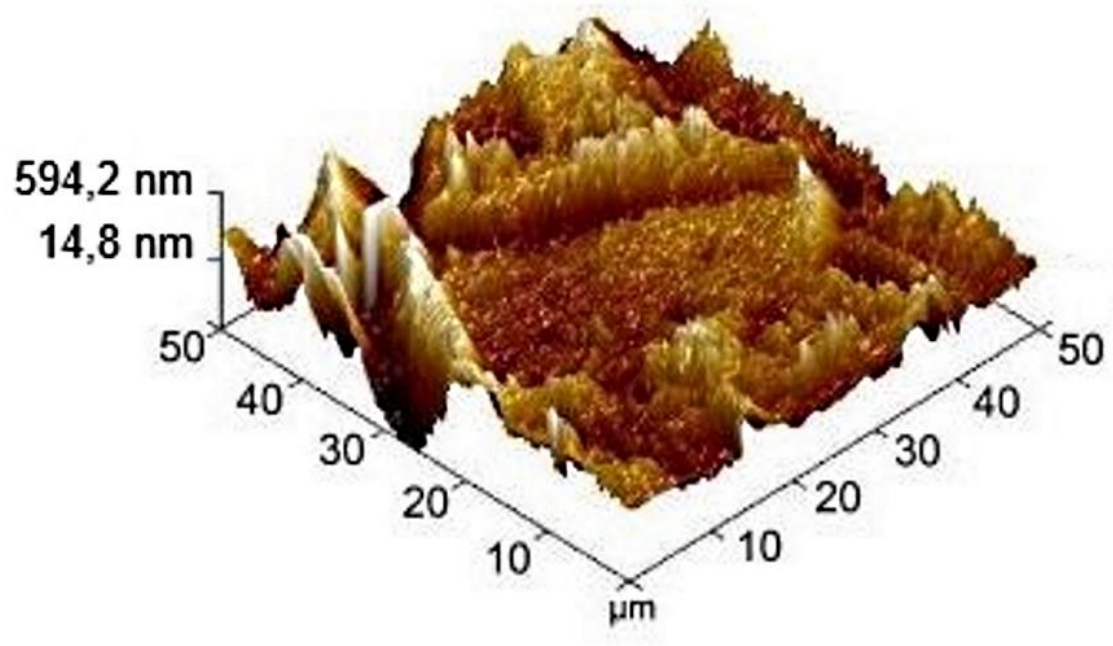

Figure 3.6. 3D image of nitrogen implanted 316 SS by AFM as a function of 90 minutes time

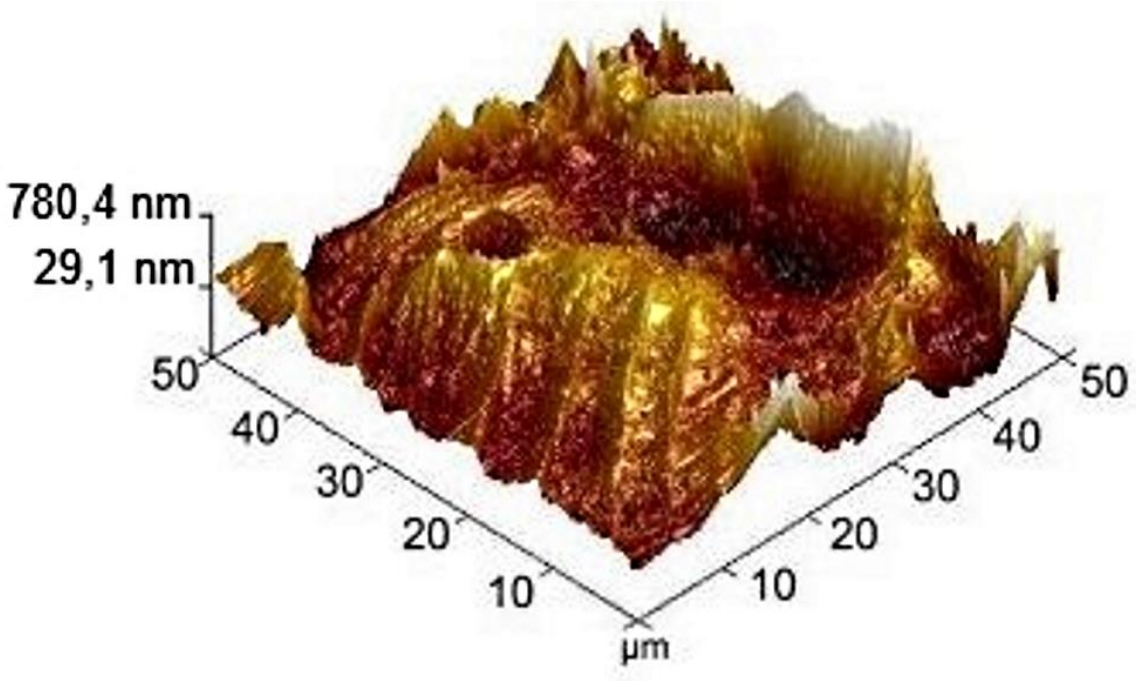

Figure 3.7. 3D image of nitrogen implanted 316 SS by AFM as a function of 240 minutes time

The average roughness gives the deviation in surface heights, while the RMS roughness represents the standard deviation of the surface heights. As can be seen from

the equations below, the RMS roughness is expected to be higher than the average roughness. The average roughness and the RMS roughness are defined by the expressions in Equation 3.1 and Equation 3.2, respectively.

$$R_q = \sqrt{\frac{1}{n}\sum_{i=1}^{n} y_i^2} \tag{3.1}$$

$$R_a = \frac{1}{n}\sum_{i=1}^{n} |y_i| \tag{3.2}$$

Table 3.3. Average and RMS roughness values of nitrided 316 SS specimen layers due to different processing time based on the AFM measurements.

	R_a (nm)			**R_q (nm)**		
	Ra_{30x30}	**Ra_{50x50}**	**$Ra_{100x100}$**	**Rq_{30x30}**	**Rq_{50x50}**	**$Rq_{100x100}$**
30 minutes	37,37	49,7	78,2	49,63	66,63	98,77
90 minutes	43,2	91,03	151,33	57,67	122,00	199,00
240 minutes	64,6	116,63	264	90,70	153,67	348,00

As can be seen from the table, the roughness of N implanted layers increases as a function of processing time. This is due to the sputtering effect of high flux nitrogen beam. Also, for each sample, both average and RMS roughness values show increase as the scanning area size enlarges. Also, the compressive stresses that the nitrogen implanted layers are under may be contributing to the increased surface roughness of the nitrogen implanted samples.

3.5. Magnetic Characterization

3.5.1. MFM Analysis Results and Discussions

In this study, domain structures of the γ_N layer of the specimens were investigated by MFM. Figure 3.8 represents the domain structure of each specimen at different scanning areas (50 x 50 μm^2 and 100 x 100 μm^2). These images were taken

sequentially over a span of several parts to look for domain structures. Besides, Figure 3.9 enables to compare both 3D and 2D images of domains at 30x30 μm^2 scanning area.

(a) 30-minutes N implanted specimen

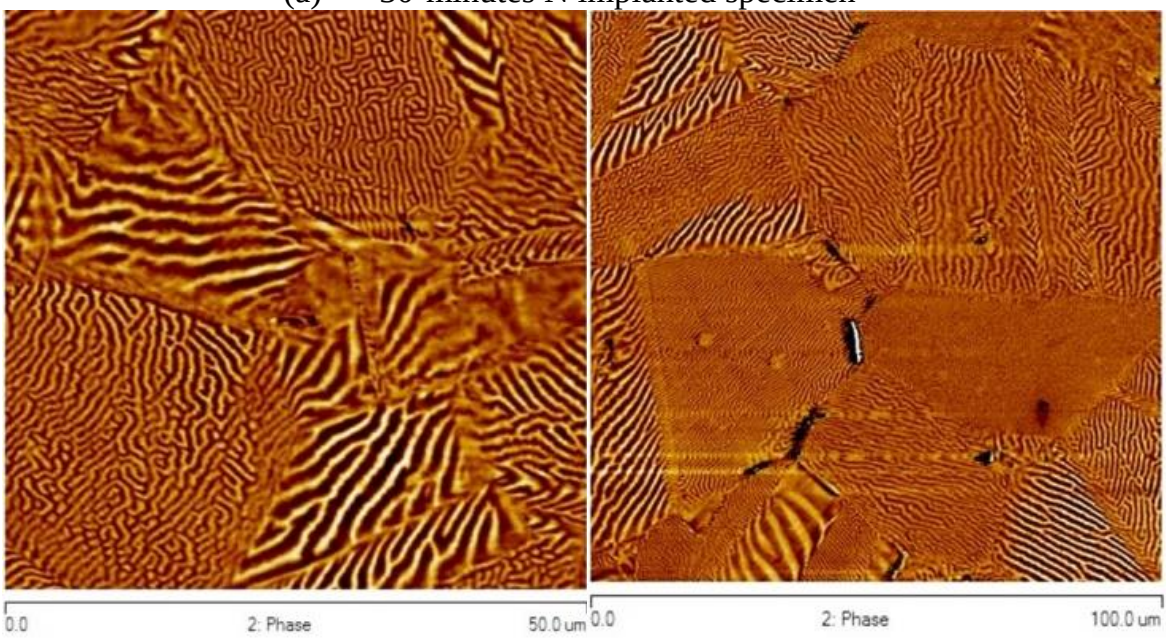

(b) 90-minutes N implanted specimen

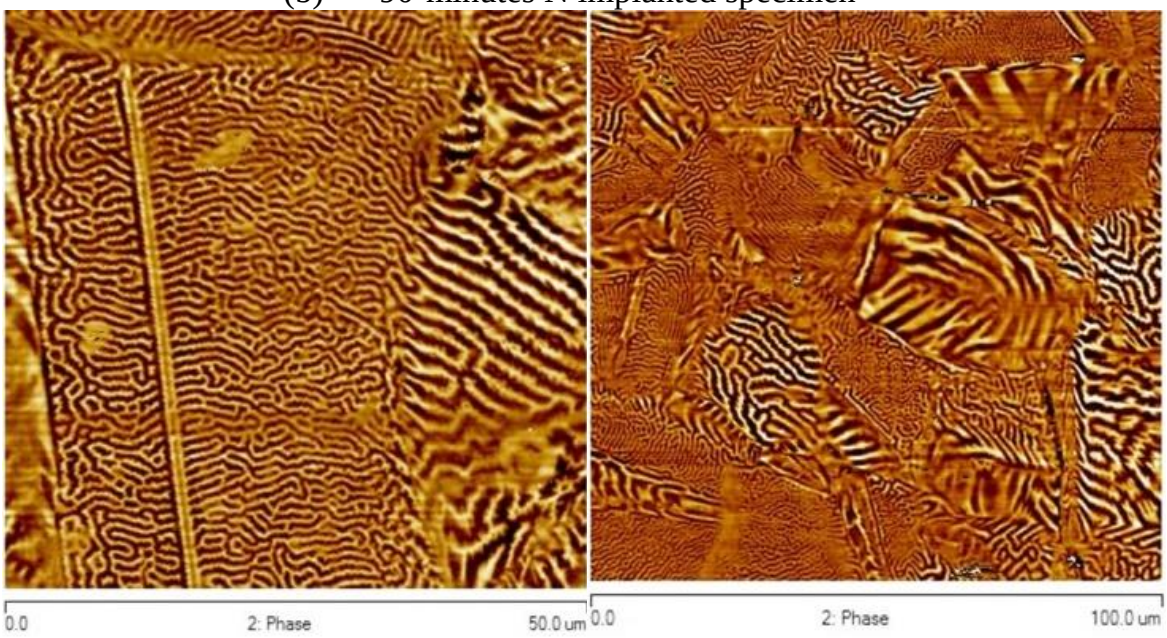

Figure 3.8. MFM images of nitrogen implanted specimens of (a) 30-minutes, (b) 90-minutes and (c) 240 minutes N implanted specimens at 50 μm^2 (left) and 100 μm^2 (right) of scanning areas.

(Cont. on next page)

(c) 240-minutes N implanted specimen

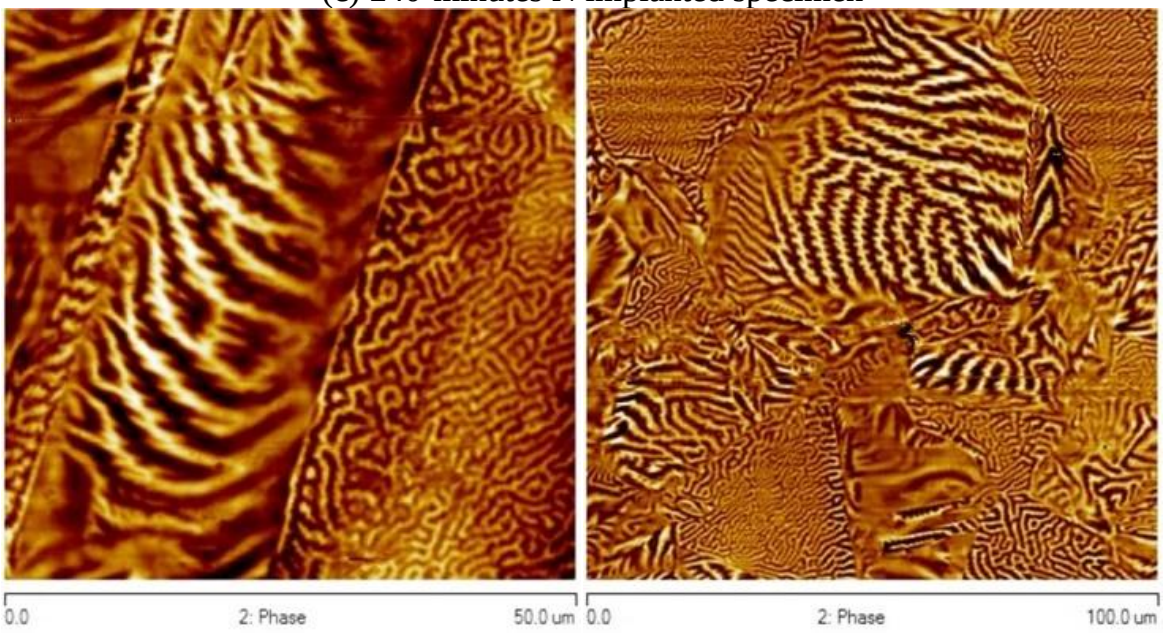

Figure 3.8. (Cont.)

From the earlier studies, ferromagnetism in γ_N layers on austenitic steels has been revealed by observation of stripe like domains structures. As can be seen from the figures, the appearance of the striped domain patterns in each image is an indication of ferromagnetism in the implanted surfaces. The results are consistent with previous studies. A study reveals that (Basso, Pimentel, Weber, Marcos, Czerwiec, Baumvol and Figueroa 2009), the nitrogen expanded austenite has two different layers, an outermost ferromagnetic layer and a paramagnetic layer beneath it. In the 3D images, a clear ferromagnetic type domain structure is observed because of this phase has N-rich regions. We can say probably paramagnetic, nitrogen-poor phase probably lies beneath the outer layer (Öztürk and Williamson 1995). On the other hand, magnetic behavior varies from one polycrystalline grain to another. This variation was explained by the non-uniform N contents and different amounts of lattice expansion in the differently oriented grains (Öztürk, Fidan and Mändl 2014). A recent plasma nitrogen implanting study of 316L polycrystalline austenitic stainless steel (via MFM and MOKE analyses) verified that the magnetic response of nitrogen-enriched grains is correlated with their crystallographic orientation (Menéndez et al., 2010; Wu et al., 2011). Additionally, as the processing time increases, height of domains increases.

(a) 30-minutes N implanted specimen

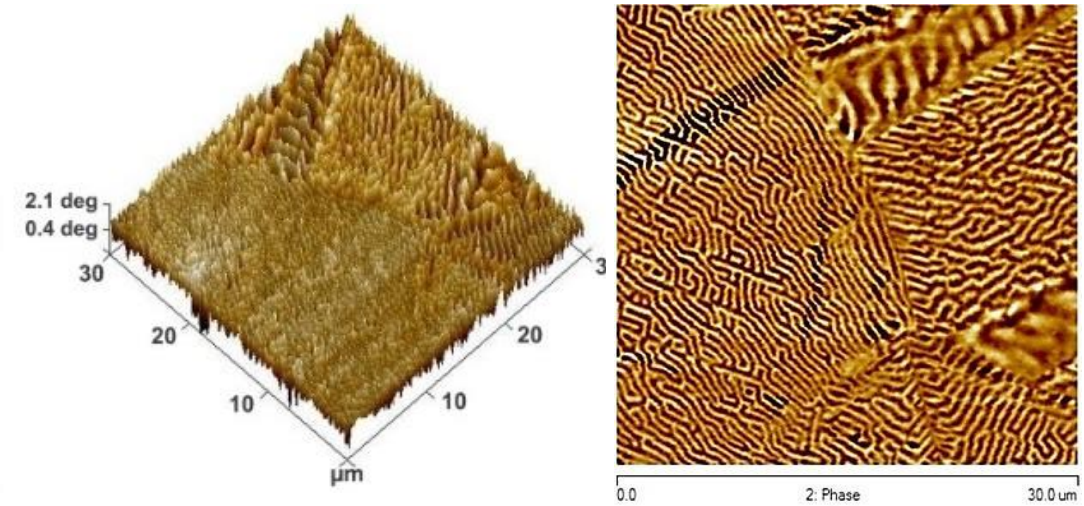

(b) 90-minutes N implanted specimen

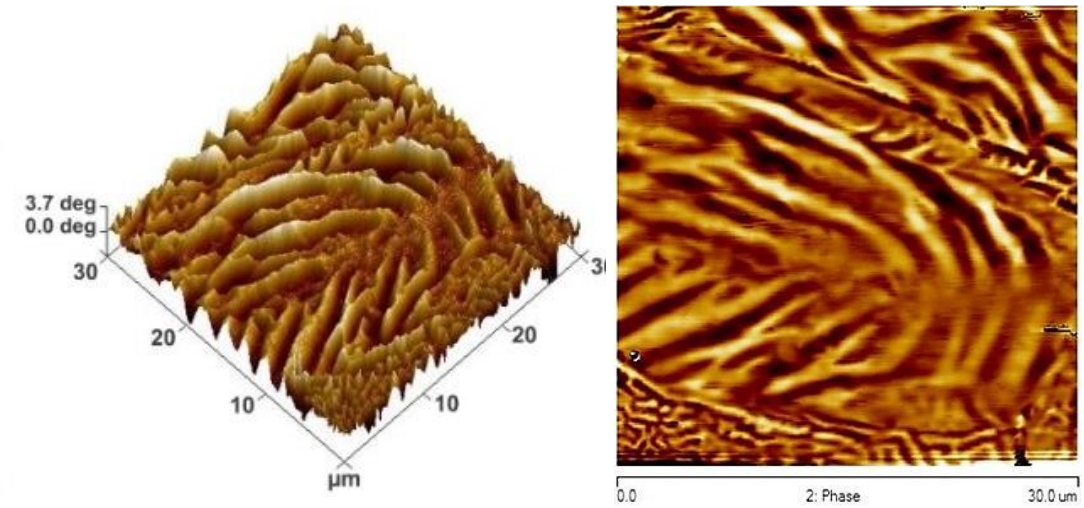

(c) 240-minutes N implanted specimen

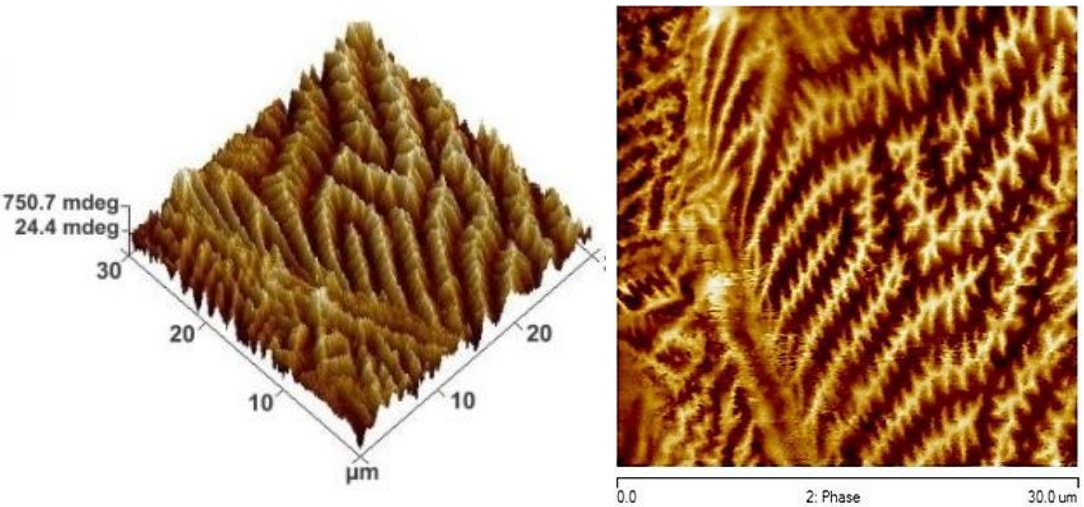

Figure 3.9. 3D (right) and 2D (left) MFM images of (a) 30-minutes, (b) 90-minutes and (c) 240 minutes N-implanted specimens at 30 μm^2 scanning area.

3.5.2. VSM Analysis Results and Discussions

The VSM measurements in this study were performed to determine both the in-plane and out-of-plane hysteresis loops of the specimens. Figure 3.10, Figure 3.11 and Figure 3.12 represent the hysteresis behavior of each specimen, 30 minutes-implantation time, 90 minutes-implantation time and 240 minutes-implantation time, respectively. Besides, Figure 3.13 provides a comparison for out-of-plane hysteresis loop behavior of each specimen.

The hysteresis loops for the each nitrogen implanted sample demonstrate ferromagnetic type behavior and suggest both out-of-plane and in-plane magnetization of the domain structure. However, lack of saturation is clearly seen for each VSM data of specimens. This can be due to contribution of the non-magnetic (paramagnetic) signals coming from the underlying substrate to the VSM data. From the VSM data, the coercive field of out-of-plane magnetization of specimens is estimated to be ~ 35, 34, 37 Gauss where in-plane magnetization of specimens is estimated to be ~ 64, 60 and 50 Gauss, respectively

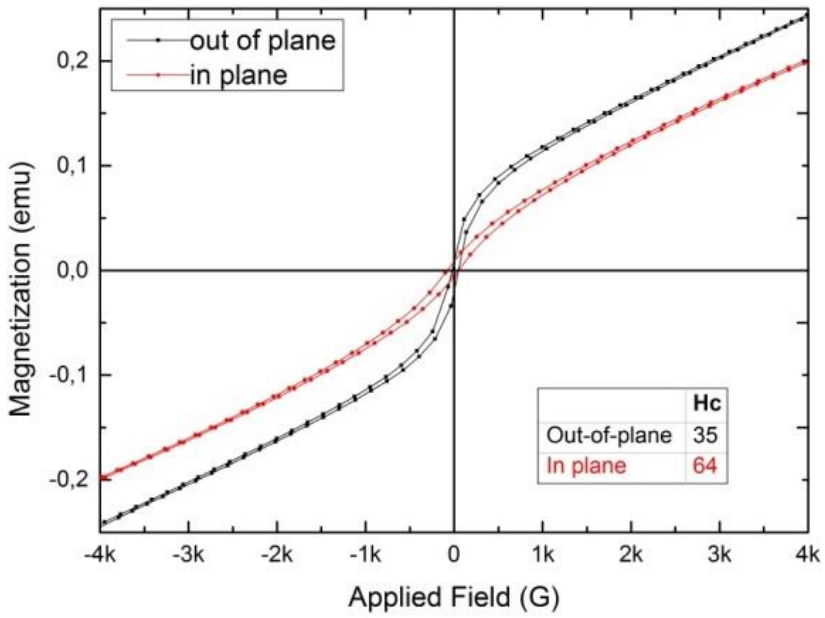

Figure 3.10. VSM data for the 30-minutes nitrogen implanted specimen.

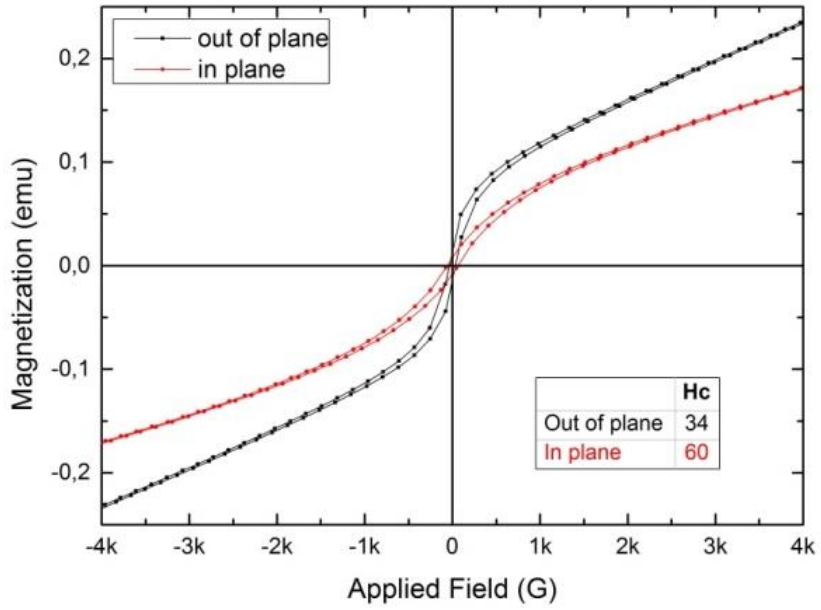

Figure 3.11. VSM data for the 90-minutes nitrogen implanted specimen

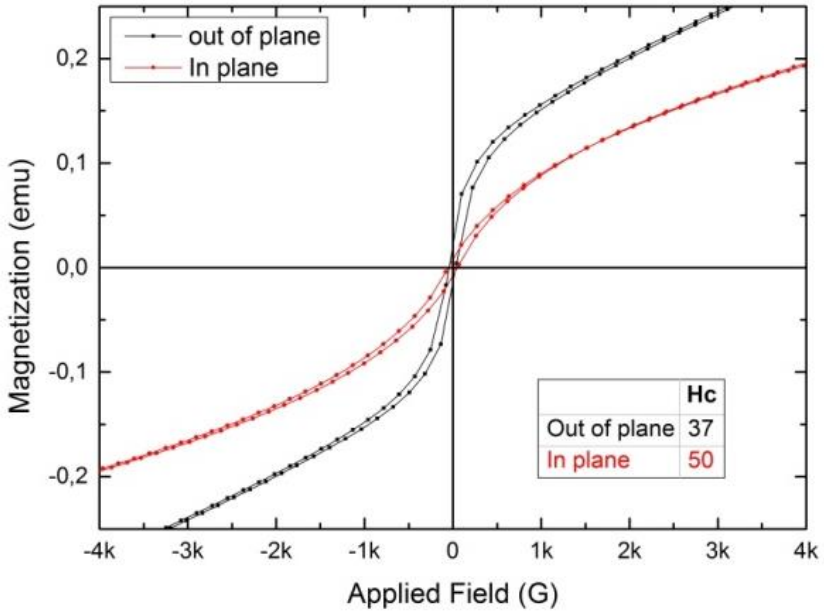

Figure 3.12. VSM data for the 240-minutes nitrogen implanted specimen

Although the MFM images of the stripe domains suggest mainly out-of-plane magnetization for the γ_N layer, the VSM analysis results imply both out-of-plane and in-plane magnetization of the domain structure. From these results, the hysteresis loops for the nitrogen ion implanted specimens indicate γ_N is a soft ferromagnet such as soft iron.

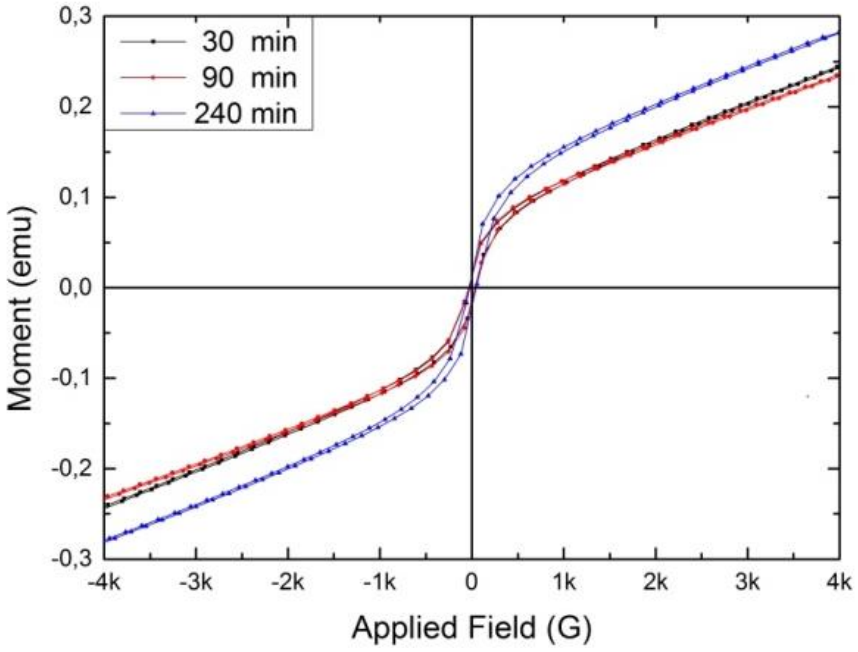

Figure 3.13. Out-of-plane VSM data of three specimens

Table 3.4. Average calculations of total area, remanent magnetization, magnetic saturation, coercivity and saturating field of samples in Out-of-plane configuration via VSM

Out-of-Plane					
	Total Area (erg)	**Remanent Magnetization, M_r (10^{-3} emu)**	**Magnetic Saturation, M_s (emu)**	**Coercivity Field, H_c (G)**	**Saturating Field, H_{sat} (G)**
30 mins	36,451	13,3	0,26	35,247	4468,51
90 mins	37,501	13,3	0,25	34,619	4453,01
240 mins	45,288	17,8	0,30	37,014	4426,35

Table 3.5. Average calculations of total area, remanent magnetization, magnetic saturation, coercivity and saturating field of samples in In-plane configuration via VSM

In-Plane					
	Total Area (erg)	**Remanent Magnetization, M_r (10^{-3} emu)**	**Magnetic Saturation, M_s (emu)**	**Coercivity Field, H_c (G)**	**Saturating Field, H_{sat} (G)**
30 mins	34,996	7,3	0,22	64,441	4411,37
90 mins	32,452	7,7	0,18	60,797	4427,32
240 mins	21,233	7,4	0,21	50,603	4440,02

3.5.3. MOKE Analyis Results and Discussions

In this study, the magnetic state of the γ_N phase was determined by a surface sensitive technique, magneto-optic Kerr rotation, MOKE. On the other hand, MOKE results could be obtained by only the first sample, 30-minutes nitrogen implanted one. As it is mentioned in previous Chapter 3.4, roughness showed increasing as the implantation time increased. This case most probably prevented to collect signals from the rough surfaces of other two specimens. Figure 3.14 shows the hysteresis behavior loop of the 30-minutes nitrogen implanted specimen.

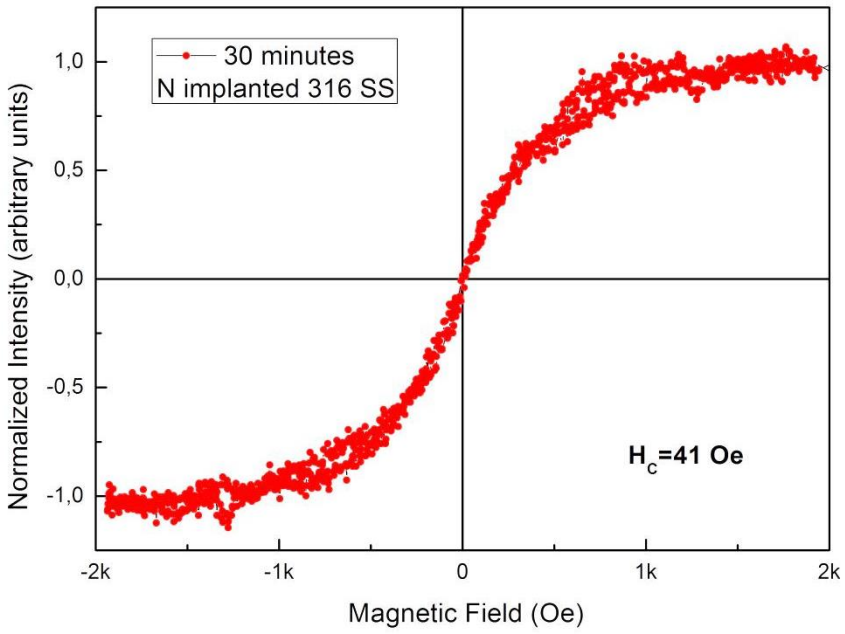

Figure 3.14. In-plane magnetization MOKE data of 30-minutes nitrogen implanted 316 SS specimen

As can be seen from this figure, MOKE data for the 30 minutes N implanted sample demonstrates ferromagnetic type behavior. The estimated coercive field is ~ 41 Oe. The sample does not have a well-defined loop structure. This can be interpreted in terms of a ferromagnetic order with a much smaller coercive field. The characteristic shown by the hysteresis loop for the implanted sample is similar to that of a softer ferromagnet such as soft iron.

CHAPTER 4

CONCLUSIONS

4.1. Summary

In this study, new data related to structural and magnetic nature of the expanded austenite layer formed on 316L SS substrate by a low-energy, high-flux nitrogen ion implantation method was investigated. Combined X-ray diffraction, SEM, AFM and MFM, VSM as well as MOKE analyses provide strong evidence for the formation of the γ_N phase, [γ_N -(Fe, Cr, Ni)], with mainly ferromagnetic characteristics. The uniform nature of the γ_N layer is clearly demonstrated by X-ray diffraction analyses. Surface imaging analyses by SEM and AFM demonstrated that the surface roughness increased as a function of time due to the sputtering effect. According to the MFM, VSM and MOKE analyses, ferromagnetism in the γ_N layer is revealed by the observation of stripe domain structures and the hysteresis loops. The MFM images show variation in the size and form of the magnetic domains from one grain to another. This is attributed mainly to the orientation of the individual grains and different amounts of the lattice expansion in the different grains as indicated from the XRD data.

4.2. Conclusions

a. A metastable, fcc, high nitrogen concentration phase (γ_N) is found to be produced in fcc 316 SS alloy for low-energy, high-flux nitrogen ion implantation for a substrate temperature near 400 ^oC.
b. 316 SS has same lattice constant at (200) and (111) planes. Although 316 SS substrate itself represents fcc crystal structure, γ_N phase represents orientation dependent, anisotropic behavior suggesting expansion of lattice. XRD results show an increase of lattice constants in (200) and (100) planes as the processing time increases. Lattice expansion percent varies from ~ 6,7 to ~ 7,8 % in (111) plane, whereas the expansion percent varies from ~ 8.9 to ~ 10 % in (200) plane. (Zhang and Bell 1985)

c. The N is found to have a higher content and to diffuse deeper in the (200) grains oriented parallel to the surface compared to the (111) grains.
d. As the implantation time increases, a significant detrimental effect is observed on the surfaces of the polycrystalline material.
e. The nitrogen ion implanted surfaces became rougher with respect to the processing time. The average roughness of each sample was calculated by AFM. Average roughness ranged from 55,09 to 148,41 as the processing time increased.
f. Nitrogen content in γ_N phase was obtained by EDX. There is no appreciable change in atomic percent of nitrogen in the layers. (~28 at.%) This manifests the existence of ferromagnetic behavior of the γ_N.
g. The MFM data presented suggests that the expanded phase magnetic behavior is changing with crystallographic orientation.
h. VSM results represent clear hysteresis loops of specimens in both in-plane and out-of-plane magnetization components.

Unfortunately MOKE analysis could not be implemented successfully for those two of samples at the processing times of 90 minutes and 240 minutes due to higher roughness. Even a well-defined hysteresis loop could not be obtained for the sample 30 minute nitrogen implanted sample, the characteristic shown by the hysteresis loop for the implanted sample is similar to that of a softer ferromagnet such as soft iron.

REFERENCES

Abrasonis, G., et al.s.2005. "Flux effect on the ion-beam nitriding of austenitic stainless-steel AISI 304L", *Journal of Applied Physics.* Vol. 97(12), pp. 124906.

Als-Nielsen, J. and D. McMorrow. 2011. *Elements of modern X-ray physics*, John Wiley & Sons.

Atkins, P. 2010. *Shriver and Atkins' inorganic chemistry*, Oxford University Press.

Basso, R. L. d. O., et al.s.2009. "Magnetic and structural properties of ion nitrided stainless steel", *Journal of Applied Physics.* Vol. 105(12), pp. 124914.

Blawert, C., et al.s.2001. "Nitrogen and carbon expanded austenite produced by PI 3", *Surface and Coatings Technology.* Vol. 136(1), pp. 181-187.

Burgei, W., et al.s.2003. "A simple vibrating sample magnetometer for use in a materials physics course", *American Journal of Physics.* Vol. 71(8), pp. 825-828.

Callister, W. D. and D. G. Rethwisch. 2012. *Fundamentals of materials science and engineering: an integrated approach*, John Wiley & Sons.

Chen, J., et al.s.2008. "Improving the wear properties of Stellite 21 alloy by plasma surface alloying with carbon and nitrogen", *Wear.* Vol. 264(3), pp. 157-165.

Collins, G., et al.s.1995. "Nitriding of austenitic stainless steel by plasma immersion ion implantation", *Surface and Coatings Technology.* Vol. 74, pp. 417-424.

Cullity, B.s.1956. "Diffraction I: the directions of diffracted beams", *Elements of X-ray diffraction, Addison-Wesley Publishing Co., Inc., USA.* Vol. 78.

Dearnley, P., et al. (1989). Surface Engineering: Proceedings of International Conference PSE, DGE.

Fewell, M., et al.s.2000. "The nature of expanded austenite", *Surface and Coatings Technology.* Vol. 131(1), pp. 300-306.

Foner, S.s.1959. "Versatile and Sensitive Vibrating-Sample Magnetometer", *Review of Scientific Instruments.* Vol. 30(7), pp. 548-557.

Ichii, K., et al.s.1986. "Structure of the ion-nitrided layer of 18-8 stainless steel", *Technol. Rep. Kansai Univ.*(27), pp. 135-144.

Izman, S., et al. 2012. *Surface modification techniques for biomedical grade of titanium alloys: Oxidation, carburization and ion implantation processes*, INTECH Open Access Publisher.

Jiang, J. and E. Meletiss.2000. "Microstructure of the nitride layer of AISI 316 stainless steel produced by intensified plasma assisted processing", *Journal of Applied Physics.* Vol. 88(7), pp. 4026-4031.

Johnson, M., et al.s.1996. "Magnetic anisotropy in metallic multilayers", *Reports on Progress in Physics.* Vol. 59(11), pp. 1409.

Martinavičius, A., et al.s.2012. "Nitrogen interstitial diffusion induced decomposition in AISI 304L austenitic stainless steel", *Acta Materialia.* Vol. 60(10), pp. 4065-4076.

Menéndez, E., et al.s.2008. "Patterning of magnetic structures on austenitic stainless steel by local ion beam nitriding", *Acta Materialia.* Vol. 56(17), pp. 4570-4576.

Menéndez, E., et al.s.2010. "Out-of-plane magnetic patterning on austenitic stainless steels using plasma nitriding", *Applied Physics Letters.* Vol. 96(24), pp. 242509.

Neves, B. and M. Andrades.1999. "Identification of two patterns in magnetic force microscopy of shape memory alloys", *Applied Physics Letters.* Vol. 74(14), pp. 2090-2092.

Öztürk, O., et al.s.2014. "MFM imaging of expanded austenite formed on 304 SS and CoCrMo alloys", *Surface and Coatings Technology.* Vol. 256, pp. 15-22.

Öztürk, O., et al.s.2009. "Structural and magnetic characterization of plasma ion nitrided layer on 316L stainless steel alloy", *Nuclear Instruments and Methods in Physics Research Section B: Beam Interactions with Materials and Atoms.* Vol. 267(8), pp. 1540-1545.

Öztürk, O. and D. Williamsons.1995. "Phase and composition depth distribution analyses of low energy, high flux N implanted stainless steel", *Journal of Applied Physics.* Vol. 77(8), pp. 3839-3850.

Poppe, L., et al.s.2001. "A laboratory manual for X-ray powder diffraction", *US Geological Survey Open-File Report.* Vol. 1(041), pp. 1-88.

Rautray, T. R., et al.s.2011. "Ion implantation of titanium based biomaterials", *Progress in Materials Science.* Vol. 56(8), pp. 1137-1177.

Riviere, J., et al.s.2002. "High current density nitrogen implantation of an austenitic stainless steel", *Surface and Coatings Technology.* Vol. 158, pp. 99-104.

Roth, J. R. 2001. *Industrial Plasma Engineering: Volume 2-Applications to Nonthermal Plasma Processing,* CRC Press.

Tian, X., et al.s.2000. "Medium-temperature plasma immersion-ion implantation of austenitic stainless steel", *Thin Solid Films.* Vol. 366(1), pp. 150-154.

Wei, R., et al.s.1994. "The effects of low-energy-nitrogen-ion implantation on the tribological and microstructural characteristics of AISI 304 stainless steel", *Journal of tribology.* Vol. 116(4), pp. 870-876.

Williamson, D., et al.s.1994. "Metastable phase formation and enhanced diffusion in fcc alloys under high dose, high flux nitrogen implantation at high and low ion energies", *Surface and Coatings Technology.* Vol. 65(1), pp. 15-23.

Williamson, D., et al.s.2001. "Role of ion-beam processing time in the formation and growth of the high-nitrogen phase in austenitic stainless steel", *BOOK-INSTITUTE OF MATERIALS.* Vol. 752, pp. 333-352.

Wozniak, M., et al.s.2005. "Magnetic properties of austeno-ferritic stainless steel after cathodic hydrogen charging", *Journal of alloys and compounds.* Vol. 404, pp. 626-629.

Wu, D., et al.s.2011. "Ferromagnetism in interstitially hardened austenitic stainless steel induced by low-temperature gas-phase nitriding", *Scripta Materialia.* Vol. 65(12), pp. 1089-1092.

Zhang, Z. and T. Bells.1985. "Structure and corrosion resistance of plasma nitrided stainless steel", *Surface Engineering.* Vol. 1(2), pp. 131-136.